ORIGINAL RESEARCH

A Point Mutation R122C in RUNX3 Promotes the Expansion of Isthmus Stem Cells and Inhibits Their Differentiation in the Stomach

Daisuke Douchi,[1,2,*] Akihiro Yamamura,[1,2,*] Junichi Matsuo,[1] Jung-Won Lee,[3] Napat Nuttonmanit,[1] Yi Hui Melissa Lim,[1] Kazuto Suda,[1,4] Mitsuhiro Shimura,[1,2] Sabirah Chen,[1] ShuChin Pang,[1] Kazuyoshi Kohu,[1] Mari Kaneko,[5] Hiroshi Kiyonari,[5] Atsushi Kaneda,[6] Hideyuki Yoshida,[7] Ichiro Taniuchi,[8] Motomi Osato,[1] Henry Yang,[1] Michiaki Unno,[2] Jimmy Bok-Yan So,[9] Khay Guan Yeoh,[10] Linda Shyue Huey Chuang,[1,§] Suk-Chul Bae,[3] and Yoshiaki Ito[1,§]

[1]Cancer Science Institute of Singapore, National University of Singapore, Singapore; [2]Department of Surgery, Tohoku University Graduate School of Medicine, Sendai, Japan; [3]Department of Biochemistry, School of Medicine, Institute for Tumor Research, Chungbuk National University, Cheongju, South Korea; [4]Department of Pediatric General and Urogenital Surgery, Juntendo University School of Medicine, Tokyo, Japan; [5]Laboratory for Animal Resources and Genetic Engineering, RIKEN Center for Biosystems Dynamics Research, Kobe, Japan; [6]Department of Molecular Oncology, Graduate School of Medicine, Chiba University, Chiba, Japan; [7]YCI Laboratory for Immunological Transcriptomics; [8]Laboratory for Transcriptional Regulation, RIKEN Center for Integrative Medical Sciences, Yokohama, Japan; [9]Department of Surgery, National University Health System; and [10]Department of Medicine, National University of Singapore, Singapore

SUMMARY

A single point mutation of RUNX3 enhanced stem cell proliferation and inhibition of differentiation to promote the development of precancerous lesions in the stomach.

BACKGROUND & AIMS: RUNX transcription factors play pivotal roles in embryonic development and neoplasia. We previously identified the single missense mutation R122C in RUNX3 from human gastric cancer. However, how RUNX3^{R122C} mutation disrupts stem cell homeostasis and promotes gastric carcinogenesis remained unclear.

METHODS: To understand the oncogenic nature of this mutation in vivo, we generated the *RUNX3^{R122C}* knock-in mice. Stomach tissues were harvested, followed by histologic and immunofluorescence staining, organoid culture, flow cytometry to isolate gastric corpus isthmus and nonisthmus epithelial cells, and RNA extraction for transcriptomic analysis.

RESULTS: The corpus tissue of *RUNX3$^{R122C/R122C}$* homozygous mice showed a precancerous phenotype such as spasmolytic polypeptide-expressing metaplasia. We observed mucous neck cell hyperplasia; massive reduction of pit, parietal, and chief cell populations; as well as a dramatic increase in the number of rapidly proliferating isthmus stem/progenitor cells in the corpus of *RUNX3$^{R122C/R122C}$* mice. Transcriptomic analyses of the isolated epithelial cells showed that the cell-cycle–related MYC target gene signature was enriched in the corpus epithelial cells of *RUNX3$^{R122C/R122C}$* mice compared with the wild-type corpus. Mechanistically, RUNX3^{R122C} mutant protein disrupted the regulation of the restriction point where cells decide to enter either a proliferative or quiescent state, thereby driving stem cell expansion and limiting the ability of cells to terminally differentiate.

CONCLUSIONS: RUNX3^{R122C} missense mutation is associated with the continuous cycling of isthmus stem/progenitor cells, maturation arrest, and development of a precancerous state. This work highlights the importance of RUNX3 in the prevention of metaplasia and gastric cancer. *(Cell Mol Gastroenterol Hepatol 2022;13:1317–1345; https://doi.org/10.1016/j.jcmgh.2022.01.010)*

Keywords: Isthmus; Stem/Progenitor Cell; Enhanced Stem Cell Activity; Preneoplastic State; Gastric Carcinogenesis.

Most current article

The most common form of gastric cancer, the intestinal type, is preceded by a cascade of precancerous lesions, such as chronic inflammation and parietal cell loss (chronic atrophic gastritis), spasmolytic polypeptide-expressing metaplasia (SPEM) and intestinal metaplasia, and dysplasia.[1,2] Commonly mutated genes in gastric cancer include *TP53*, *ARID1A*, and Kirsten rat sarcoma viral oncogene homolog (*KRAS*), as well as genes in the Wingless-type MMTV integration site family (WNT; ie, *APC* and *CTNNB1*) and transforming growth factor β (TGF-β) pathways (ie, *SMAD4* and *SMAD2*).[3] Gastric cancers frequently are associated with *Helicobacter pylori* and Epstein–Barr virus infections. Promoter hypermethylation and transcriptional silencing of CDKN2A (p16INK4A) and MLH1 have been observed in Epstein–Barr virus–positive gastric cancer.[3] *H pylori* infection also is associated with increased levels of aberrant DNA methylation, in particular, RUNX family transcription factor 3 (RUNX3) hypermethylation, in the gastric mucosa.[4,5] RUNX3 hypermethylation has been observed in chronic gastritis, with a progressive methylation increase in intestinal metaplasia and gastric cancer.[5,6]

RUNX genes encode transcription factors that function as master developmental regulators and frequently are associated with cancer.[7] Although RUNX1 and RUNX2 are associated intimately with hematopoiesis/leukemia and osteogenesis/bone cancer, respectively, the roles of RUNX3 seem to be more diverse.[8–10] RUNX3 is highly expressed in hematopoietic cells, especially lymphocytes and the peripheral nervous system, whereas its expression in epithelial cells is generally low. However, it has been shown that RUNX3 is a potent tumor suppressor in epithelial cancers because *Runx3* knockout mice showed increased proliferation and hyperplasia of gastric epithelial cells.[10,11] Furthermore, the chemical carcinogen N-methyl-N-nitrosourea induced adenocarcinomas more frequently in fundic and pyloric glands of 52-week-old *Runx3*-deficient mice than in wild-type (WT) mice, suggesting that Runx3 loss is a central event in precancerous state induction in the stomach.[12] Moreover, heterozygous inactivation of Runx3 in mice induced adenomas in the intestine, lung, and mammary gland.[13] Altogether, these data indicate that RUNX3 plays critical roles in suppressing the fundamental mechanisms of cancer initiation.

Mechanistically, RUNX3 is linked directly to core regulatory pathways such as the cell-cycle restriction points, TGF-β, signal transducer and activator of transcription (STAT), WNT, and Yes-associated protein 1 (YAP) signaling. Through its interaction with the TGF-β effectors SMAD2/3, RUNX3 promotes TGF-β–mediated growth suppression and apoptosis through the transcriptional activation of CDKN1A (also known as p21) and BCL2L11 (BIM).[14,15] In the intestine, RUNX3 attenuates oncogenic WNT signaling by interacting with and inhibiting the transactivational potential of the WNT effectors Transcription factor 4 (TCF4)–β-catenin.[16] Therefore, APC and RUNX3 may function independently as gatekeepers in colon adenoma development. The interaction of RUNX3 with TEAD4 inhibits the oncogenic

TEAD–YAP complex.[17] Moreover, RUNX3 interacts with STAT5, resulting in the mutual inhibition of their transcriptional activity.[18] RUNX3 also has been reported to regulate cell-cycle progression after mitogenic stimulation; RUNX3 forms a complex with BRD2 in a KRAS-dependent manner, resulting in the induction of p14ARF (CDKN2A) and CDKN1A expression in the early phase of the cell cycle.[19] In the presence of the oncogenic KRAS, RUNX3 activates the CDKN2A–p53 pathway, ultimately leading to apoptosis.[19]

Epigenetic inactivation of RUNX3 is common in solid tumors.[7] Although infrequent, mutations in the *RUNX3* gene have been detected in gastric cancer. Our group identified the substitution of arginine 122 to cysteine in the DNA-binding Runt domain of RUNX3 (termed a RUNX3^R122C mutation).[11] The RUNX3^R122C mutant cannot bind adequately to DNA and fails to transactivate cell-cycle–inhibitor CDKN1A.[14] Exogenous expression of WT RUNX3 in a gastric cancer cell line strongly inhibited the tumor growth in nude mice, which contrasted with large tumor formation when RUNX3^R122C mutant was inoculated.[11]

The growth-inhibitory activities of RUNX3 is linked to several major signaling pathways implicated in gastric carcinogenesis. Understanding how a single amino acid substitution is enough to disrupt the tumor-suppressor activity of RUNX3 is crucial to elucidate the molecular mechanisms underlying gastric carcinogenesis. To this end, we generated a *RUNX3^R122C* mutant mice line. The stomachs of *RUNX3^R122C/R122C* homozygous mice showed precancerous characteristics and a dramatic increase in the isthmus stem/progenitor cells with incomplete terminal differentiation. Mechanistically, the dysfunction of a cell-cycle restriction point in *RUNX3^R122C* mice promoted continuous proliferation of stem/progenitor cells, which ultimately led to a precancerous state.

Results

Expression of Runx3 Transcripts in the Gastric Corpus Tissue

Anatomically, the mouse stomach can be roughly subclassified into 3 parts: forestomach, corpus, and antrum. RNA in situ hybridization (ISH) showed endogenous *Runx3* messenger RNA (mRNA) expression in the *Cdh1*-positive cells of the corpus of the WT mice (Figure 1*A–C*). The corpus gland is subdivided into 4 regions: pit, isthmus, neck, and base regions. Stem/progenitor cells are located in the isthmus region of the corpus gland, and mitotic activity is confined to this region. The base region consists of nonproliferative zymogenic chief cells. By performing ISH, *Runx3* mRNA was found in the epithelial cells of both isthmus and basal regions (Figure 1*D*).

Precancerous Metaplasia Development in the Corpus of 6-Month-Old RUNX3^R122C/R122C Mice

To evaluate the function of RUNX3^R122C in the stomach, we generated the conventional *RUNX3^R122C* C57BL/6 inbred strain knock-in mice (Figure 2). We systemically evaluated
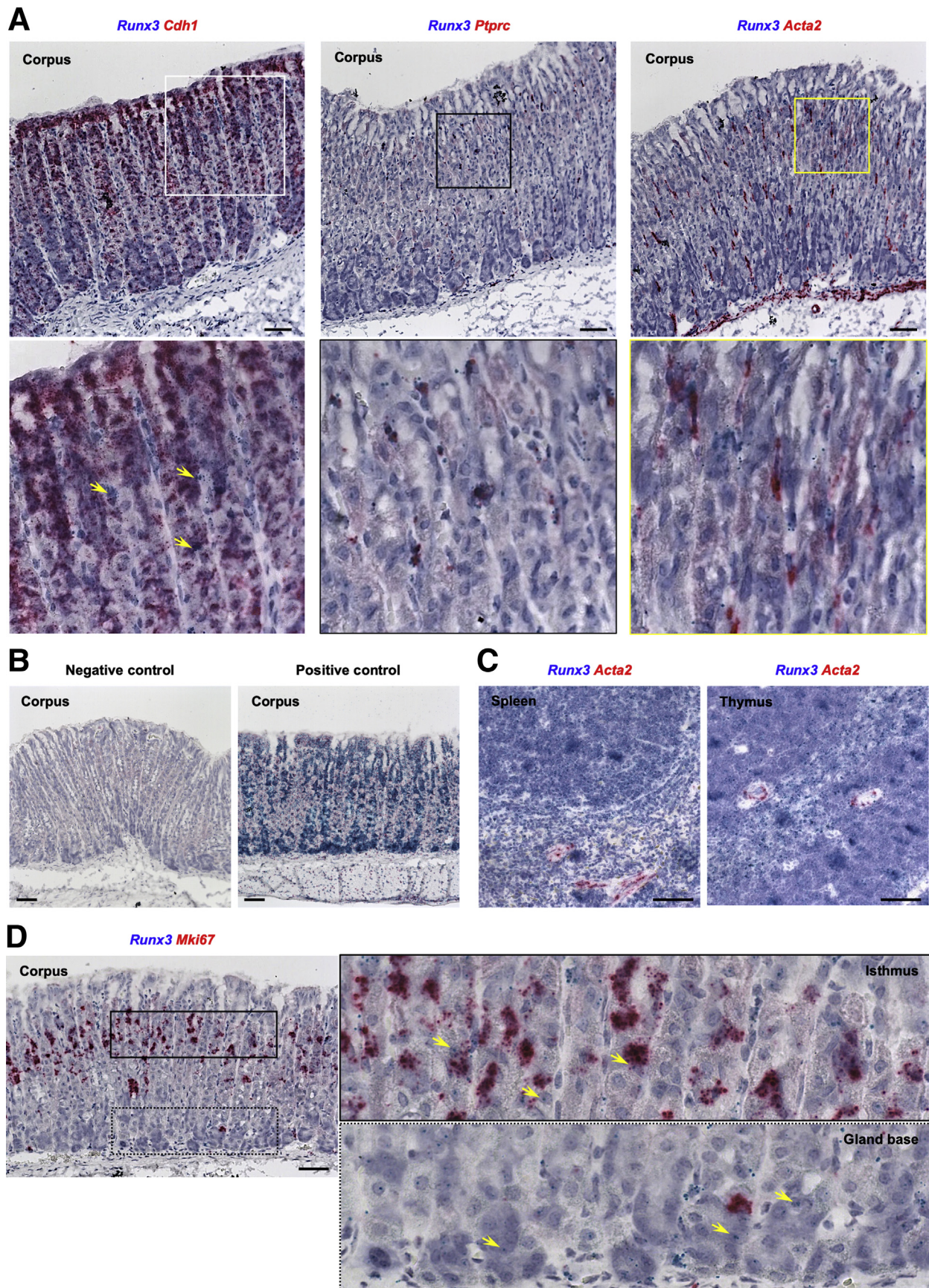
Figure 1. The expression profile of the *Runx3* gene in the corpus of WT mice. (*A*) ISH for *Runx3* and *Cdh1*, *Ptprc*, or *Acta2* in the corpus of WT mice. *Yellow arrows* indicate *Runx3* mRNA expression. (*B*) ISH for negative and positive control in the corpus of WT mice. (*C*) ISH for *Runx3* and *Acta2* in the spleen and thymus of WT mice. (*D*) ISH for *Runx3* and *Mki67* in the corpus of WT mice. *Boxes* indicate enlarged regions. *Yellow arrows* indicate *Runx3* mRNA expression within epithelial cells at the isthmus (*top panel*) and basal (*bottom panel*) regions. *Scale bars*: 50 μm.
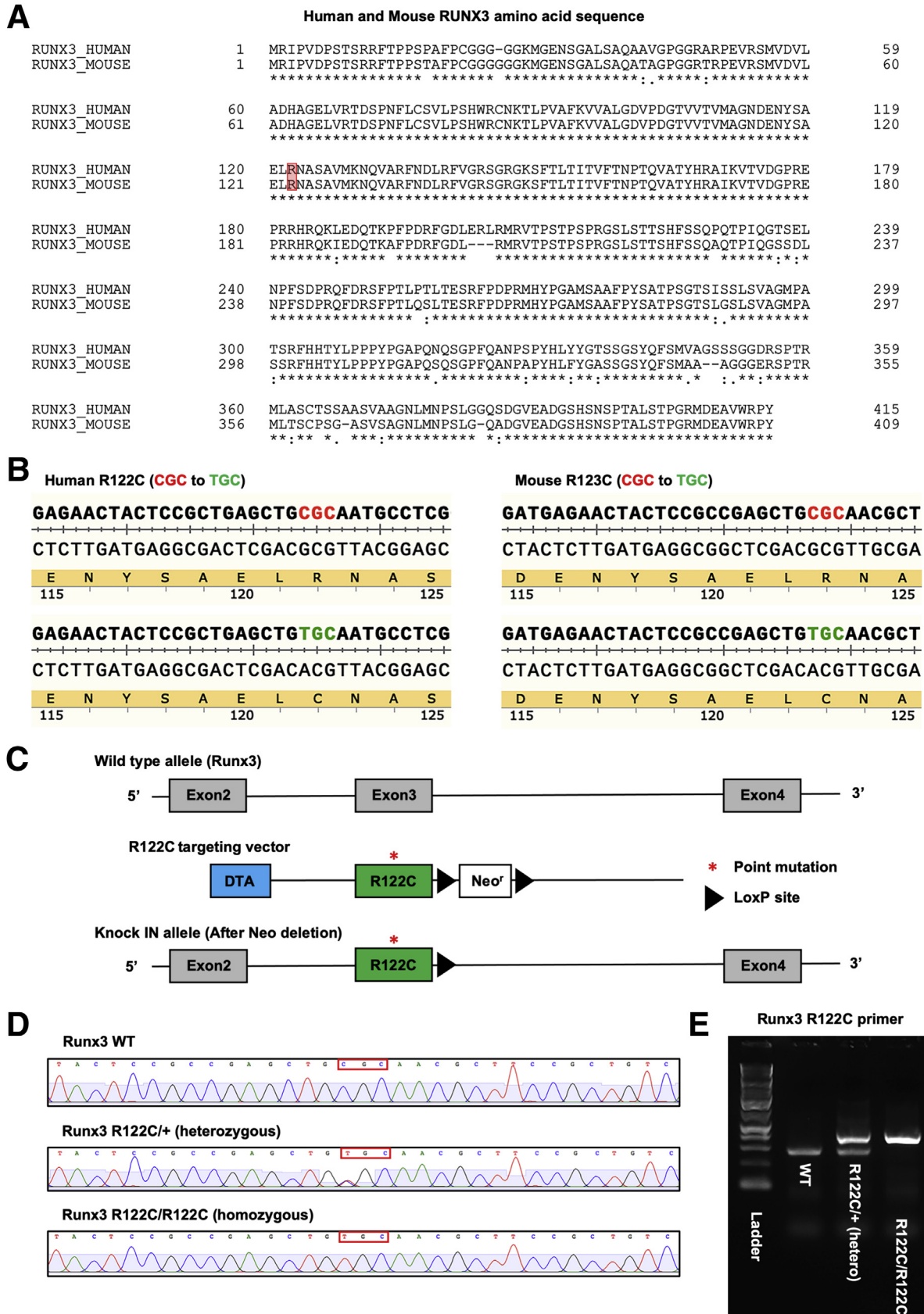
Figure 2. Generation of the conventional *RUNX3^R122C* knock-in mice. (*A*) Human (*above*) and mouse (*below*) RUNX3/Runx3 amino acid sequence. (*B*) Human RUNX3 R122C (CGC to TGC) is equivalent to mouse Runx3 R123C (CGC to TGC). (*C*) Knock-in strategy for the generation of the *RUNX3^R122C* mouse model. (*D*) Fragment of the Runx3 sequence in WT, *RUNX3^R122C/+* (heterozygous), and *RUNX3^R122C/R122C* (homozygous) mice. (*E*) Genotyping of WT, *RUNX3^R122C/+* (heterozygous), and *RUNX3^R122C/R122C* (homozygous) mice. DTA, diphtheria toxin A; LoxP, locus of X-over P1; Neo, neomycin.
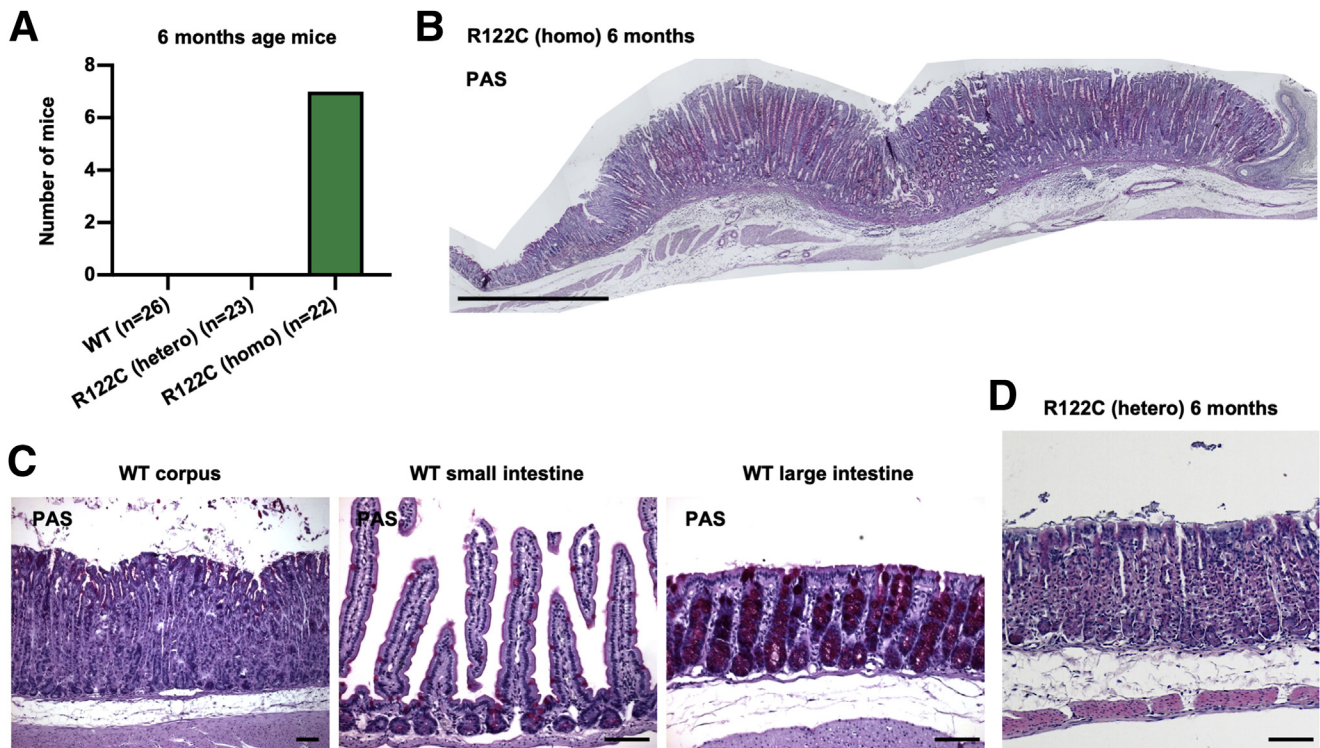
Figure 3. Characteristics of the corpus tissue of 6-month-old WT and *RUNX3^{R122C/R122C}* mice. (*A*) The numbers of mice of different genotypes showing phenotype in the corpus. (*B*) Periodic acid–Schiff (PAS) staining of the corpus of 6-month-old *RUNX3^{R122C/R122C}* mice. (*C*) PAS staining of the corpus, small intestine, and large intestine of WT mice. (*D*) H&E staining of the corpus of 6-month-old *RUNX3^{R122C/+}* heterozygous mice. *Scale bars*: 1 mm (*B*), 50 μm (*C* and *D*).

the corpus tissue of *RUNX3^{R122C}* mice at 6–8 weeks and 6 months of age compared with that of similar-aged WT mice. The stomachs of WT, *RUNX3^{R122C/+}* heterozygous, and *RUNX3^{R122C/R122C}* homozygous mice at 6–8 weeks of age (>15 mice each) showed normal gastric morphology. By contrast, the stomachs of *RUNX3^{R122C/R122C}* mice at 6 months of age showed the presence of conspicuous macroscopic lesions in 7 of the 22 mice (Figure 3A). The phenotype was entirely absent in the other *RUNX3^{R122C/R122C}* mice. The *RUNX3^{R122C/+}* mice and WT mice at 6 months of age showed normal morphology (Figures 3A and D, and 4A and B). H&E and periodic acid–Schiff staining of the lesions indicated mucous neck cell hyperplasia in the corpus of *RUNX3^{R122C/R122C}* mice (Figures 3B and C, and 4B). A similar ratio, that is, 2 of 5 *RUNX3^{R122C/R122C}* mice older than 1 year, showed the same phenotype.

To evaluate the characteristics of the hyperplastic region in *RUNX3^{R122C/R122C}* mice, we stained the stomach sections with antibodies against the hydrogen potassium adenosine triphosphatase (ATPase) α subunit (Atp4a) (a parietal cell marker). In the expanded fundic region of *RUNX3^{R122C/R122C}* mice, the number of mature parietal cells—as reflected by Atp4a expression—were decreased markedly, relative to WT mice (Figure 4C and E). By contrast, *Griffonia simplicifolia* lectin II (GSII) (a mucous neck cell marker) staining indicated a dramatic increase of mucous neck cells in the fundic area of *RUNX3^{R122C/R122C}* mice (Figure 4C and E). Although gastric intrinsic factor (GIF) (a chief cell marker) and mucin 5ac (Muc5ac) (a pit cell marker) were normally

expressed in the mature chief cells and pit cells of WT mice, their levels were reduced in *RUNX3^{R122C/R122C}* mice (Figure 4D). The number of mature chief cells also was decreased markedly in the fundic area of *RUNX3^{R122C/R122C}* mice (Figure 4E). Moreover, the changes in mRNA expression of *Muc6*, *Atp4a*, *Cblif* (*Gif*), and *Muc5ac* in whole corpus tissues reflected immunofluorescence (IF) staining results (Figures 4F and 5A).

The inflammatory milieu promotes metaplastic changes in the stomach. Significant inflammatory cellular infiltration in the submucosa was detected in the stomachs of 6-month-old *RUNX3^{R122C/R122C}* mice (Figure 4G). Moreover, above the muscularis mucosa, inflammatory cellular infiltration was observed in the gland base. IF staining also showed an increase in the number of CD45+ cells throughout the corpus glands of *RUNX3^{R122C/R122C}* mice (Figures 4H and 5B). The number of CD68-positive and F4/80-positive macrophage cells, which promote metaplastic transition, was increased in the gland base of *RUNX3^{R122C/R122C}* mice (Figure 5C and D). There are reports that the M2-type macrophage is an important immune subset causing preneoplastic metaplasia.[20,21] The majority of macrophages in *RUNX3^{R122C/R122C}* mice were M2 macrophages (F4/80+/CD163+), whereas there were only a few M1 macrophages (F4/80+/CD163-) (Figure 5E). WT mice, by contrast, have relatively much fewer macrophages, most of which were M1 macrophages (F4/80+/CD163-) (Figure 5E).

Gastric mucous metaplasia and dysplasia are caused, in part, by interleukin (IL)6, tumor necrosis factor α (TNF-α),
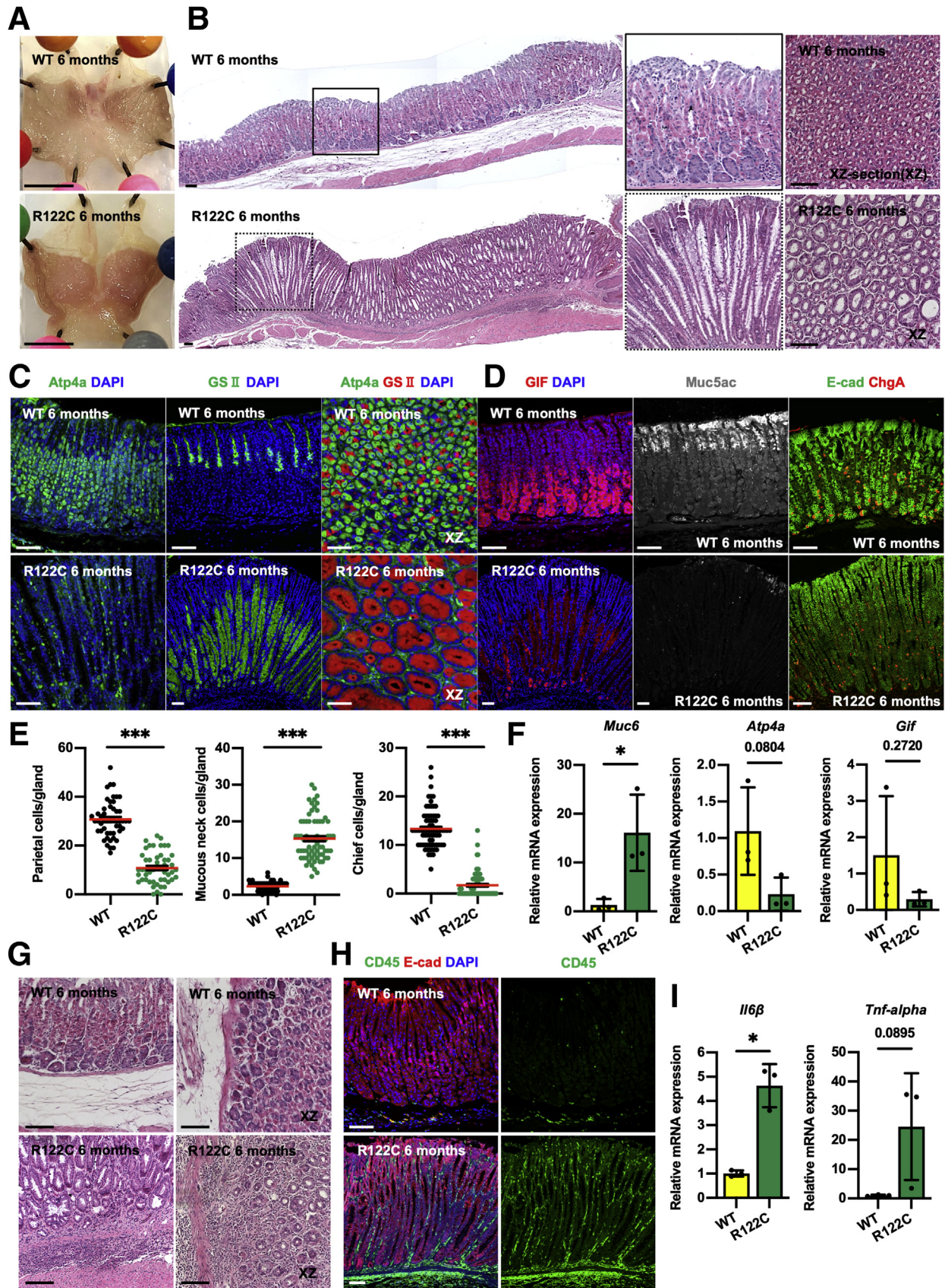
IL1β, and cyclooxygenase 2–dependent inflammation.[22,23] Quantitative polymerase chain reaction (qPCR) showed that the mRNA expression of the inflammation markers was increased in the corpus of RUNX3[R122C/R122C] mice at 6 months of age compared with those of age-matched WT mice (Figures 4I and 5F). Interestingly, these prominent inflammatory infiltrates observed in RUNX3[R122C/R122C] mice on a C57BL/6 background contrasted with the absence of significant inflammatory cell infiltration in 6-month-old Runx3-deficient mice on a BALB/c background.[12]

Characterization of the Isthmus Stem/Progenitor Cells From RUNX3[R122C/R122C] Mice

Tissue stem cells are characterized by multipotency and the ability to self-renew. In the corpus glands of WT mice, proliferation was observed mainly in the isthmus region (Figure 6A). Most of these isthmus stem/progenitor cells expressed Ki67. Notably, in the corpus of 6-month-old RUNX3[R122C/R122C] mice, Ki67+ proliferating cells appeared throughout the gland, with the majority in the isthmus (Figure 6A). The number of Ki67+ cells in RUNX3[R122C/R122C] mice was approximately 5 times more than that of WT mice (Figure 6B). GSII and GIF-positive cells also had Ki67-expressing cells (Figures 6C and D, and 7). Although chief cells can undergo proliferation, this occurrence is very rare and hardly observed in homeostatic conditions (Figure 7). This implies that the multiple lineages of cells show an inherent stemness that enables the glands to efficiently respond to environmental and metaplastic changes. This observation is consistent with the fact that mucous neck cells and chief cells may acquire plasticity to give rise to a premetaplastic cell type under chronic inflammation conditions.[24]

RUNX3 is a key regulator of tissue-resident immune cells (eg, memory CD8+ T cells, natural killer cells, macrophages, and innate lymphoid cells), which may regulate the behavior of stem cells under normal physiological conditions or work together with inflammatory immune cells during stress.[25–27] It is conceivable that the R122C mutation affects the communication of immune cells with epithelial cells. To assess the change in gastric epithelial cell and stem cell properties in the RUNX3[R122C/R122C] mice in the absence of immune cells, we derived organoids from the corpus gland of WT and RUNX3[R122C/R122C] mice. Relative to WT, we observed that the RUNX3[R122C/R122C] corpus formed organoids of larger sizes and at a higher frequency (Figure 6E–G). This strongly suggests that the RUNX3[R122C/R122C] corpus showed the enhanced stem/progenitor cell activity compared with WT mice.

To identify alterations in the gene expression in the corpus of RUNX3[R122C/R122C] mice, RNA sequencing (RNA-seq) was performed using RNA isolated from the whole corpus tissues of 6-month-old WT and RUNX3[R122C/R122C] mice. Gene set enrichment analysis (GSEA) showed 14 positively and 3 negatively enriched gene sets with a false discovery rate of less than 0.05 (Figure 6H and I). Pathways related to inflammation and immunity such as interferon (IFN)-α/γ, IL6_Janus kinase_STAT3, TNF-α, IL2_STAT5, and inflammatory response were enriched in the RUNX3[R122C/R122C] corpus tissue (Figures 6H and 8A). IFN-γ has been shown to be a critical promoter of parietal cell atrophy, and, furthermore, is required for progression to metaplasia.[28] It could be that increased IFN-γ signaling in the RUNX3[R122C/R122C] mice contributed significantly to the parietal cell loss and the accompanying metaplastic changes. Moreover, E2F, MYC, G2M checkpoint, and DNA repair genes signatures, which are related to the cell cycle, were enriched in the RUNX3[R122C/R122C] corpus tissue (Figure 6H): the up-regulation of pro-proliferative genes such as BIRC5, PLK1, and MYC reflected the highly proliferative state of RUNX3[R122C/R122C] corpus tissue (Figure 8B). The reduction of Hedgehog signaling likely is owing to the loss of sonic hedgehog–expressing parietal cells in RUNX3[R122C/R122C] corpus tissue (Figure 6I). Of note, GSEA also showed the enrichment of early gastric cancer gene signature in the RUNX3[R122C/R122C] corpus tissue (Figure 6J).[29]

Therefore, the oncogenic activity of RUNX3[R122C] might stem from the ability of RUNX3[R122C] stem/progenitor cells to initiate the gastric carcinogenic processes.

Characterization of the Metaplastic Glands Using SPEM Markers

The histologic changes during chronic atrophy often are referred to as SPEM. Canonical SPEM glands are characterized by the dramatic emergence of metaplastic cells, which co-express both chief cell markers and mucous neck cell markers such as trefoil factor 2 (TFF2) and Muc6.[30] To identify columnar metaplastic cells in the RUNX3[R122C/R122C] mice fundic mucosa, we immunostained the corpus with antibodies against TFF2. The elongated fundic metaplastic mucosal glands were dominated by intensely stained TFF2-expressing cells with high proliferation compared with WT mice (Figures 9A and B, and 10A). SRY-box transcription factor 9 (Sox9) is associated with stem/progenitor cells in many organs. Although Sox9 expression in the corpus of WT mice was located predominantly at the isthmus, the metaplastic glands of RUNX3[R122C/R122C] mice showed a marked

---

Figure 4. (*See previous page*). **Characteristics of the corpus tissue of 6-month-old RUNX3[R122C/R122C] mice.** (*A*) Representative macroscopic images of the corpus of 6-month-old WT and RUNX3[R122C/R122C] mice. (*B*) H&E staining of the corpus of 6-month-old WT and RUNX3[R122C/R122C] mice. (*C*) IF staining for Atp4a and GSII in the corpus. (*D*) IF staining for GIF, Muc5ac, E-cadherin (E-cad), and chromogranin A (ChgA) in the corpus. (*E*) Quantification of the numbers of parietal, mucous neck, and chief cells per gland in the corpus tissues of 6-month-old WT and RUNX3[R122C/R122C] mice. (*F*) qPCR for *Muc6*, *Atp4a*, and *Gif* expression levels in the corpus tissues of 6-month-old WT and RUNX3[R122C/R122C] mice (n = 3 mice each). (*G*) H&E staining of the gland base in 6-month-old WT and RUNX3[R122C/R122C] mice. (*H*) IF staining for CD45 and E-cad in the corpus tissues of 6-month-old WT and RUNX3[R122C/R122C] mice. (*I*) qPCR for *Il6β* and *Tnf* expression levels in the corpus tissues of 6-month-old WT and RUNX3[R122C/R122C] mice (n = 3 mice each). *Scale bars*: 5 mm (*A*), 100 μm (*B–D*, *G*, and *H*). Data are presented as the means ± SEM and were analyzed by the Student t test. *P < .05, ***P < .001. DAPI, 4',6-diamidino-2-phenylindole.
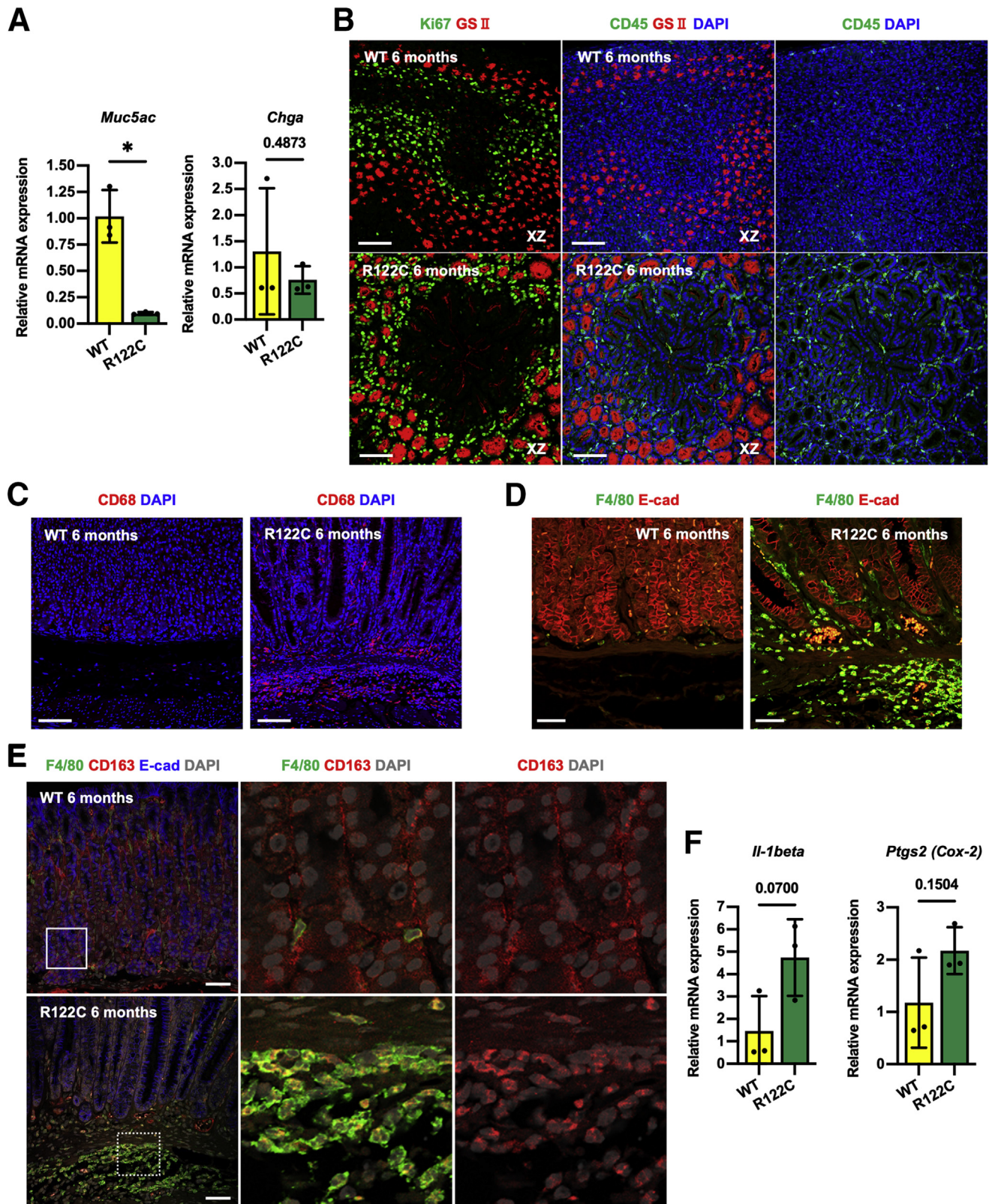
Figure 5. Features of the corpus tissue of 6-month-old *RUNX3^R122C/R122C* **mice.** (*A*) qPCR for *Muc5ac* and *Chga* expression levels in the corpus tissues of 6-month-old WT and *RUNX3^R122C/R122C* mice (*n* = 3 mice each). (*B*) IF staining (XZ-section) for Ki67, GSII, and CD45 in the corpus tissues of 6-month-old WT and *RUNX3^R122C/R122C* mice. (*C* and *D*) IF staining for (*C*) CD68 and (*D*) F4/80 and E-cad in the corpus tissues of 6-month-old WT and *RUNX3^R122C/R122C* mice. (*E*) IF staining for F4/80, CD163, and E-cad in the corpus tissues of 6-month-old WT and *RUNX3^R122C/R122C* mice. (*F*) qPCR for *Il1b* and *Ptgs2* (*Cox-2*) expression levels in the corpus tissues of 6-month-old WT and *RUNX3^R122C/R122C* mice (*n* = 3 mice each). *Scale bars*: 100 μm (*B*, *C*, and *E*), 50 μm (*D*). Data are presented as the means ± SEM and were analyzed by the Student *t* test. *$P < .05$. DAPI, 4',6-diamidino-2-phenylindole.
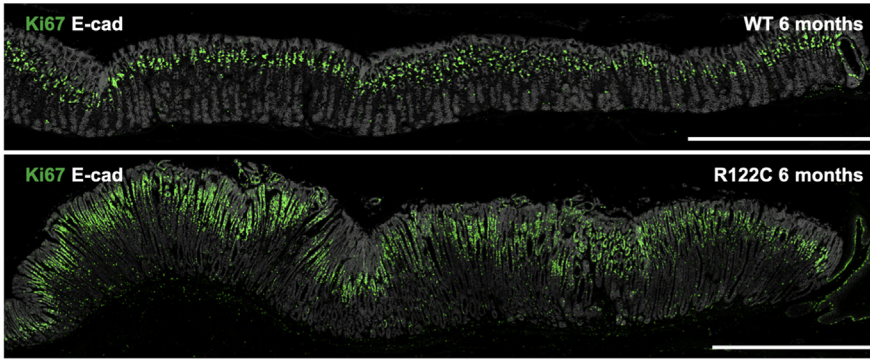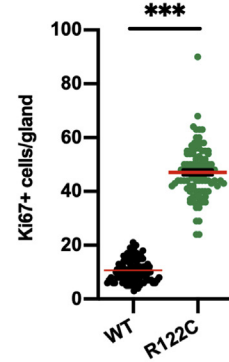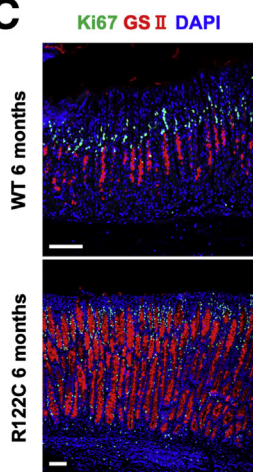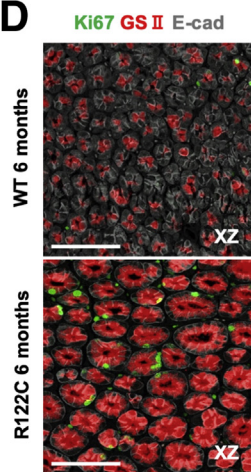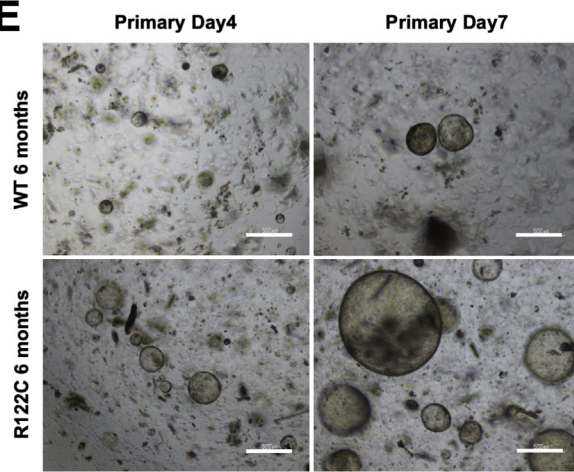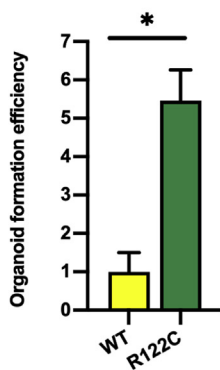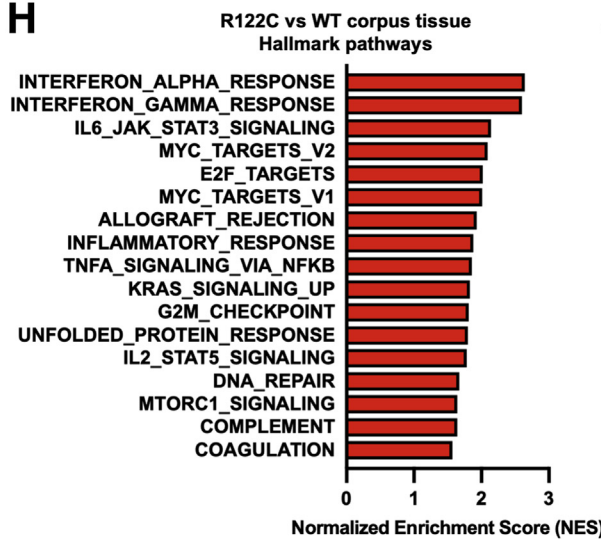
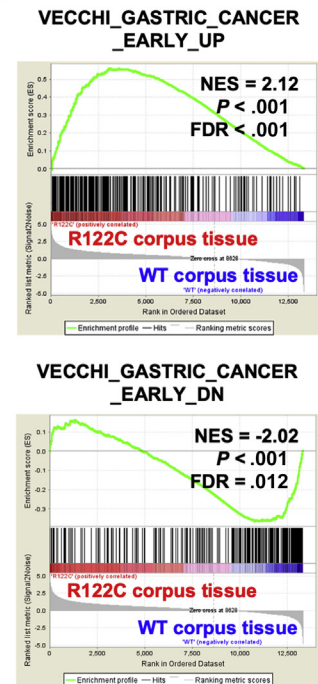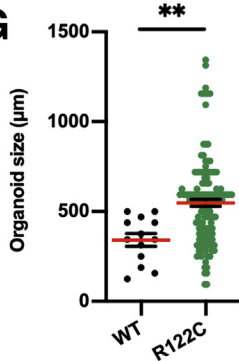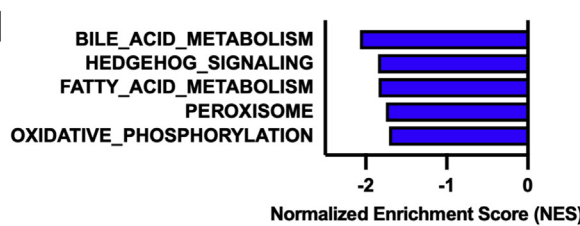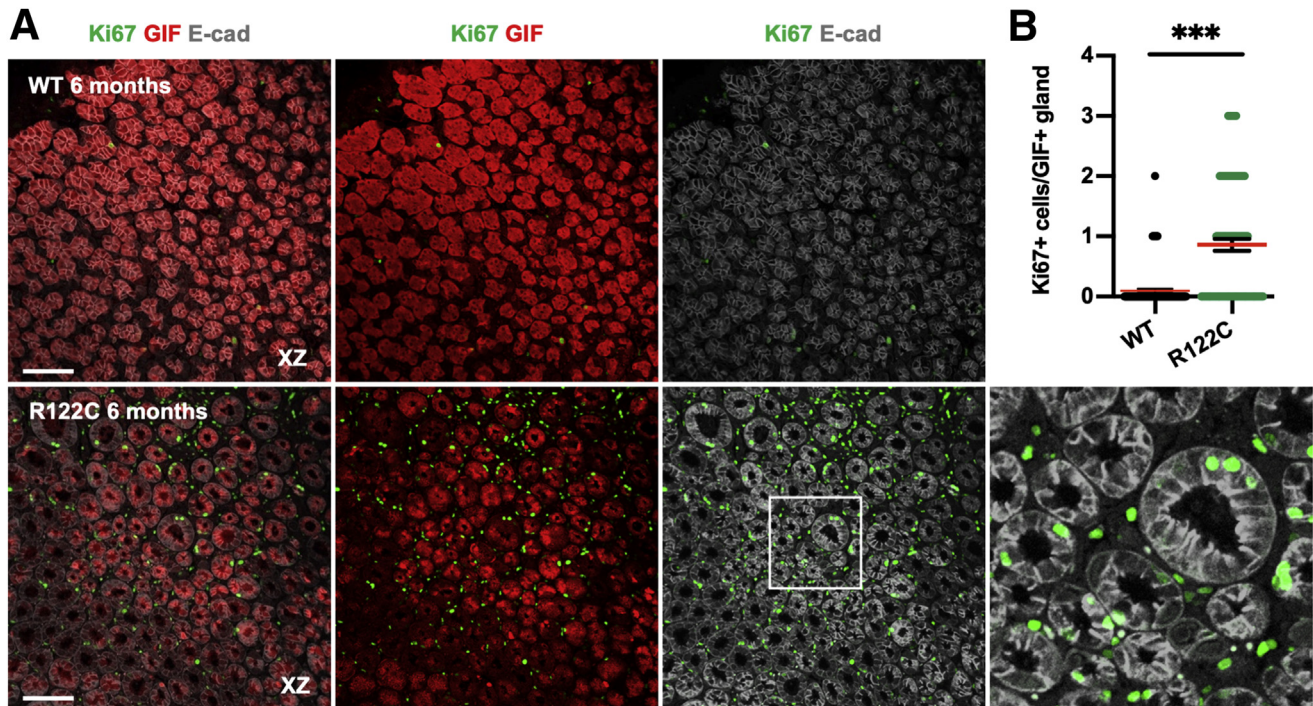**Figure 7. Characteristics of the gland base of 6-month-old WT and *RUNX3^{R122C/R122C}* mice.** (*A*) IF staining (XZ-section) for Ki67, GIF, and E-cad in the gland basal tissues of 6-month-old WT and *RUNX3^{R122C/R122C}* mice. (*B*) Quantification of the number of Ki67$^+$ cells per GIF$^+$ gland in 6-month-old WT and *RUNX3^{R122C/R122C}* mice. *Scale bars*: 100 μm. Data are presented as the means $\pm$ SEM and were analyzed by the Student *t* test. ****P* < .001. *Box* indicates enlarged region.

increase in Sox9 expression (Figure 10*B* and *C*). GSEA of RNA-seq of whole corpus tissues collected from WT and *RUNX3^{R122C/R122C}* mice showed the enrichment of TFF2 targets gene signature in the *RUNX3^{R122C/R122C}* corpus tissue (Figure 9*C*). qPCR showed that the mRNA expression of SPEM markers *Tff2*, *Cd44*, and *Gkn3* were increased in the corpus of *RUNX3^{R122C/R122C}* mice at 6 months of age compared with that of WT mice (Figure 9*D*).[24] Cells co-expressing GIF and GSII were observed at the gland base (Figure 9*E*). In sharp contrast to WT mice, CD44v10 was robustly induced in the metaplastic gland of *RUNX3^{R122C/R122C}* mice (Figure 9*F* and *G*). Furthermore, SPEM-specific molecules (*Wfdc*, *Cftr*, and *Gpx2*) were increased significantly in the corpus of *RUNX3^{R122C/R122C}* mice at 6 months of age (Figure 9*H*).

Villin is an actin-bundling protein found in the apical brush border of absorptive tissue.[31] It is expressed throughout the small intestine and antrum of WT mice (Figure 11*A*). Although villin rarely is expressed in the corpus of WT mice, the corpus of *RUNX3^{R122C/R122C}* mice showed the emergence of Villin-expressing cells (Figure 11*A* and *B*). Moreover, PDX1 was specifically expressed in the antrum of WT mice (Figure 10*E*). The expression of PDX1 was increased markedly in the corpus of *RUNX3^{R122C/R122C}* mice (Figure 10*F* and *G*). Common intestinal markers such as Muc2, Caudal type homeobox (CDX2), and CDX1 were not detected in the corpus of *RUNX3^{R122C/R122C}* mice, indicating antralization of the corpus of *RUNX3^{R122C/R122C}* mice (Figure 11*C*).

Taken together, the IF staining patterns indicated the emergence of the SPEM phenotype in the corpus of *RUNX3^{R122C/R122C}* mice. It is likely that hyperproliferation of isthmus stem/progenitor cells, coupled with reprogramming of chief cells, resulted in the acquisition of an antral-

Figure 6. (*See previous page*). **Enhanced stem/progenitor cell activity in the corpus of 6-month-old *RUNX3^{R122C/R122C}* mice.** (*A*) IF staining for Ki67 and E-cad in the corpus tissues of 6-month-old WT and *RUNX3^{R122C/R122C}* mice. (*B*) Quantification of the number of Ki67$^+$ cells per gland unit in the corpus. (*C*) IF staining for Ki67 and GSII in the corpus. (*D*) IF staining for Ki67, GSII, and E-cad in the corpus. (*E*) Microscopic image of corpus organoids derived from the corpus tissues of 6-month-old WT and *RUNX3^{R122C/R122C}* mice. (*F* and *G*) Organoid formation efficiency and size of corpus organoids derived at 7 days of organoid primary culture (*n* = 3 mice each). (*H* and *I*) GSEA using hallmark gene sets from the Molecular Signatures Database. (*H*) *Red bars* indicate the pathways enriched in the 6-month-old *RUNX3^{R122C/R122C}* corpus tissues and (*I*) *blue bars* indicate those enriched in the 6-month-old WT corpus tissues (*n* = 3 mice each). The statistically significant signatures were selected (*P* < .05; false discovery rate [FDR] < 0.05). (*J*) GSEA showing enrichment of early gastric cancer gene signatures in the corpus of 6-month-old *RUNX3^{R122C/R122C}* mice (*n* = 3 mice each). *Scale bars*: 1 mm (*A*), 100 μm (*C* and *D*), and 500 μm (*E*). Data are presented as the means $\pm$ SEM and were analyzed by the Student *t* test. **P* < .05, ***P* < .01, ****P* < .001. DAPI, 4',6-diamidino-2-phenylindole; JAK, Janus kinase.
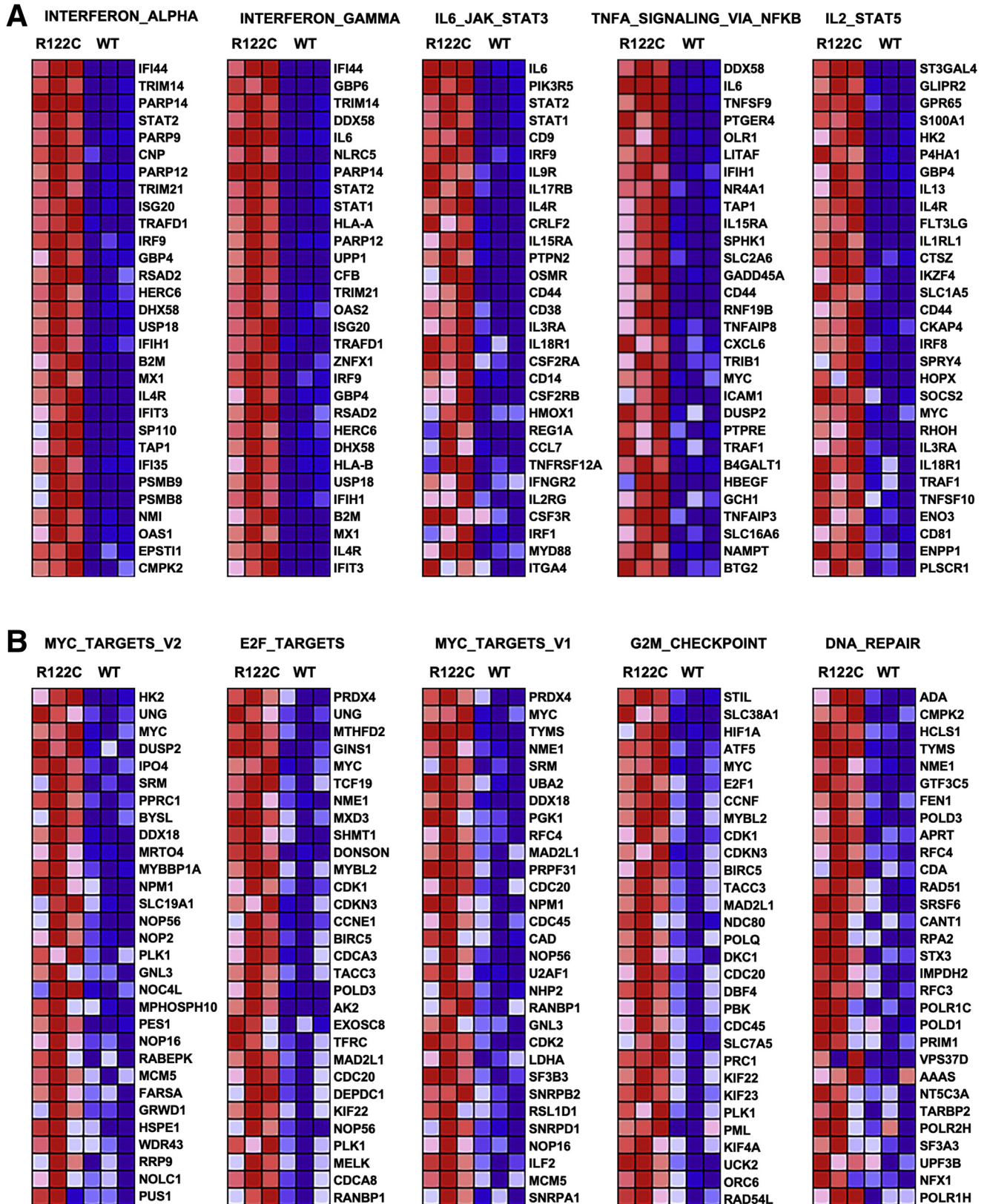
Figure 8. Enriched biological pathways of the hallmark gene sets in the corpus tissue of 6-month-old *RUNX3*$^{R122C/R122C}$ mice. (*A*) Heat map showing the top 30 genes up-regulated of IFN-α/γ, IL6_Janus kinase_STAT3, TNF-α, and IL2_STAT5 gene signatures ($n = 3$ mice each). (*B*) Heat map showing the top 30 genes up-regulated of E2F, MYC, G2M checkpoint, and DNA repair gene signatures ($n = 3$ mice each).
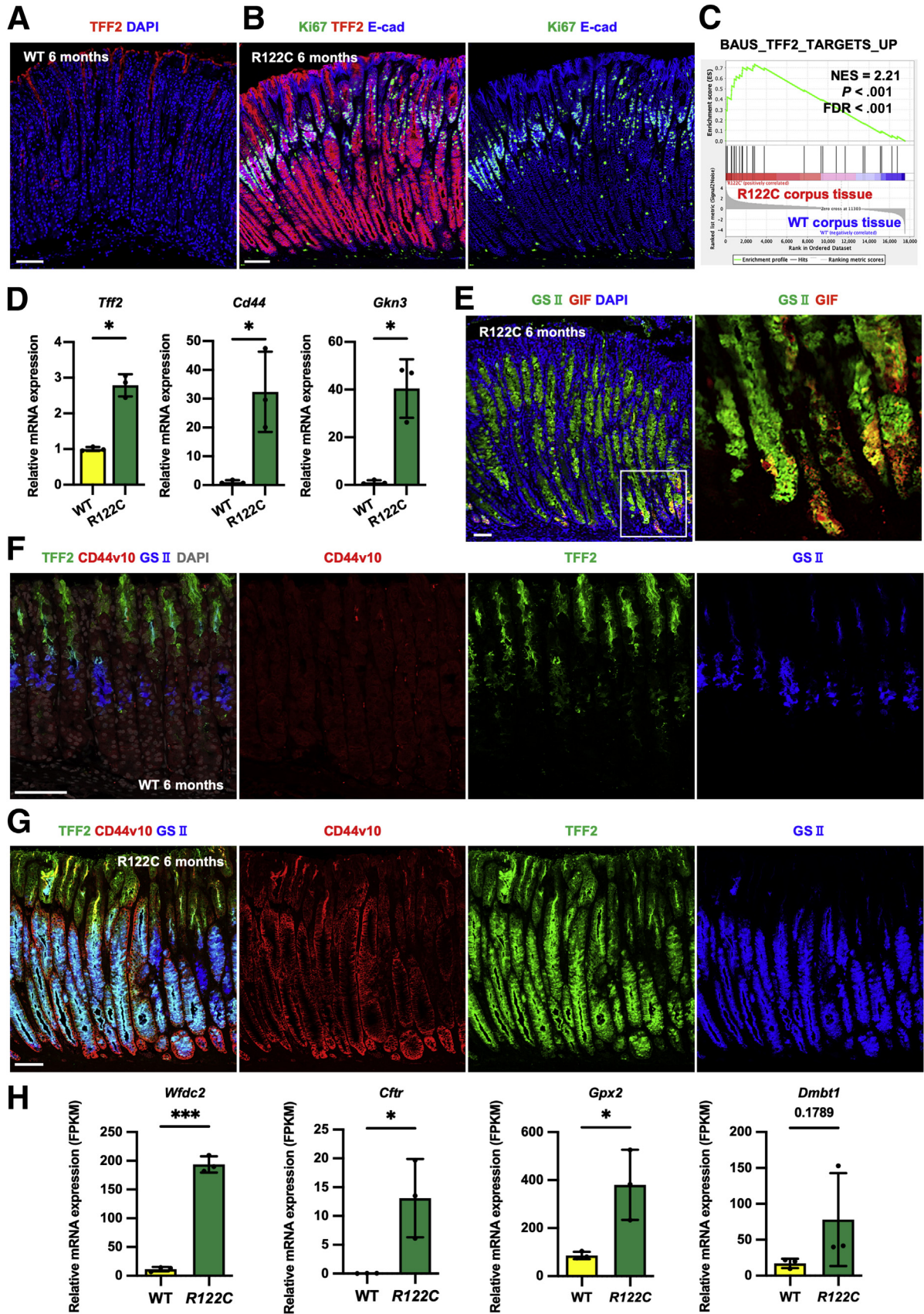
type mucosa, albeit without mature foveolar cells, in the corpus of *RUNX3*[R122C/R122C] mice.

Isthmus Stem/Progenitor Cell Sorting From *RUNX3*[R122C/R122C] Mice Using IQ motif containing GTPase activating protein 3-2A-tdTomato Reporter Mice

IQ motif containing GTPase activating protein 3 (IQGAP3) was found to be explicitly expressed in proliferative isthmus stem/progenitors in the corpus.[32] A majority of Ki67+ cells in both WT and *RUNX3*[R122C/R122C] mice coexpressed IQGAP3, suggesting that functional isthmus stem/progenitor cells were increased in 6-month-old *RUNX3*[R122C/R122C] mice compared with WT mice (Figure 12).

To further analyze the function of isthmus stem/progenitor cells of *RUNX3*[R122C/R122C] mice, we crossed *RUNX3*[R122C/R122C] mice with *Iqgap3-2A-tdTomato* reporter mice to generate *RUNX3*[R122C/R122C];*Iqgap3-2A-tdTomato* (*Runx3*[R122C];*Iqgap3-tdTomato*) mice, which showed robust tdTomato expression in Ki67+ cells in the isthmus (Figure 13A–C).[32] The 6- to 8-week-old *Runx3*[R122C];*Iqgap3-tdTomato* mice did not show any macroscopic phenotype in the corpus tissue compared with control mice, suggesting no major phenotypic changes in the young mice (Figure 13D–F). Then, we isolated Iqgap3-tdTomato[high] or Iqgap3-tdTomato[low/neg] Epithelial cell adhesion molecule (EpCAM)[high] epithelial cells of *Runx3*[WT];*Iqgap3-2A-tdTomato* (control) and *Runx3*[R122C];*Iqgap3-tdTomato* mice using 6- to 8-week-old mice, using flow cytometry (Figure 13G and H).

GSEA of RNA-seq confirmed robust up-regulation of E2F targets, Myc targets, and mitotic spindle signatures in the Iqgap3-tdTomato[high] fraction in both control and *Runx3*[R122C];*Iqgap3-tdTomato* mice, respectively (Figure 14A–C). These transcriptional signatures are consistent with the fact that Iqgap3-tdTomato[high] fraction comprised mainly isthmus stem/progenitor cells. Subsequently, we compared Iqgap3-tdTomato[high] or Iqgap3-tdTomato[low/neg] fractions in control and *Runx3*[R122C];*Iqgap3-tdTomato* mice, respectively. Notably, the results showed that Myc-target signatures were up-regulated in all of the epithelial fractions (EpCAM[high]), including the Iqgap3-tdTomato[low/neg] fraction, of *Runx3*[R122C];*Iqgap3-tdTomato* mice compared with control mice (Figures 14D, F, H and I, and 15A and C). Moreover, IFN-α/γ response and TNF-α signaling via nuclear factor-κB signatures were down-regulated in all epithelial fractions of

Runx3[R122C];*Iqgap3-tdTomato* mice (Figures 14E and G, and 15B and D).

The enrichment of the cell-cycle–related gene signatures in the corpus epithelial cells of *RUNX3*[R122C/R122C] mice likely fuels the proliferation of precancerous lesions, giving rise to mucous neck cell hyperplasia. One study reported that regulation of stemness is performed in the intestinal stem cells via IFN signaling.[33] Therefore, we should consider the possibility that the down-regulation of IFN-α/γ response signatures in the stem cells initially induces the precancerous state.

The Restriction Point Was Deregulated in *RUNX3*[R122C]-Transfected Human Embryonic Kidney cells 293 Cells

In addition to strong involvement in cell growth, apoptosis, and metabolism, Myc-target genes play key roles in cell-cycle checkpoint networks including the restriction point (R-point).[34] The R-point is a cell-cycle checkpoint in the G_1 phase.[35] Deregulation of the R-point is a common event in almost all cancer cells.[35] Under normal physiological conditions, cell proliferation is regulated by the R-point. After the R-point decision, the cell in early G_1 either retreats from the active cycle into G_0 or advances into late G_1, and the remaining phases of the cell cycle. R-point is involved in the proliferation–differentiation program of progenitor cells.[36]

Lee et al[37] identified RUNX3 as a pioneer factor for the R-point and showed that RUNX3 attenuates aberrant persistence of Ras activity by regulating R-point decision. When Ras is activated by normal mitogenic stimulation, RUNX3 forms a complex with p300, Retinoblastoma protein (pRb), and Bromodomain containing 2 (BRD2) in an mitogen-activated protein kinase activity-dependent manner. Loss of RUNX3 results in the deregulation of the R-point.[38] Under such conditions, oncogenic stimuli are not counteracted by the RUNX3–BRD2 complex. As a consequence, cells enter prematurely into the S phase, resulting in an unscheduled commitment to the cell-cycle entry.[39] RUNX3 plays a critical role in R-point regulation and preventing tumorigenesis. Formation of the RUNX3–BRD2 complex is R-point–specific and crucial to the regulation of the lineage-specific R-point decision making.[40]

To determine whether RUNX3[R122C] interacts with BRD2, we co-transfected Myc-tagged wild-type RUNX3 (Myc-

Figure 9. (*See previous page*). **Characterization of metaplastic glands.** (*A*) IF staining for TFF2 in the corpus of 6-month-old WT mice. (*B*) IF staining for Ki67, TFF2, and E-cad in the corpus of 6-month-old *RUNX3*[R122C/R122C] mice. (*C*) GSEA showing enrichment of TFF2 targets up signature in the 6-month-old *RUNX3*[R122C/R122C] corpus tissue compared with the 6-month-old WT tissue (n = 3 mice each). (*D*) qPCR for *Tff2*, *Cd44*, and *Gkn3* expression levels in the corpus tissues of 6-month-old WT and *RUNX3*[R122C/R122C] mice (n = 3 mice each). (*E*) IF staining for GSII and GIF in the corpus of 6-month-old *RUNX3*[R122C/R122C] mice. (*F and G*) IF staining for TFF2, CD44v10, and GSII in the corpus tissues of 6-month-old (*F*) WT and (*G*) *RUNX3*[R122C/R122C] mice. (*H*) The relative expression of *Wfdc2*, *Cftr*, *Gpx2*, and *Dmbt1* from RNA-seq data of the corpus tissues of 6-month-old WT and *RUNX3*[R122C/R122C] mice (n = 3 mice each). *Scale bars*: 100 μm. *Box* indicates enlarged region. Data are presented as the means ± SEM and were analyzed by the Student *t* test. *P < .05, ***P < .001. FPKM, fragments per kilobase of exon per million reads mapped. DAPI, 4',6-diamidino-2-phenylindole.
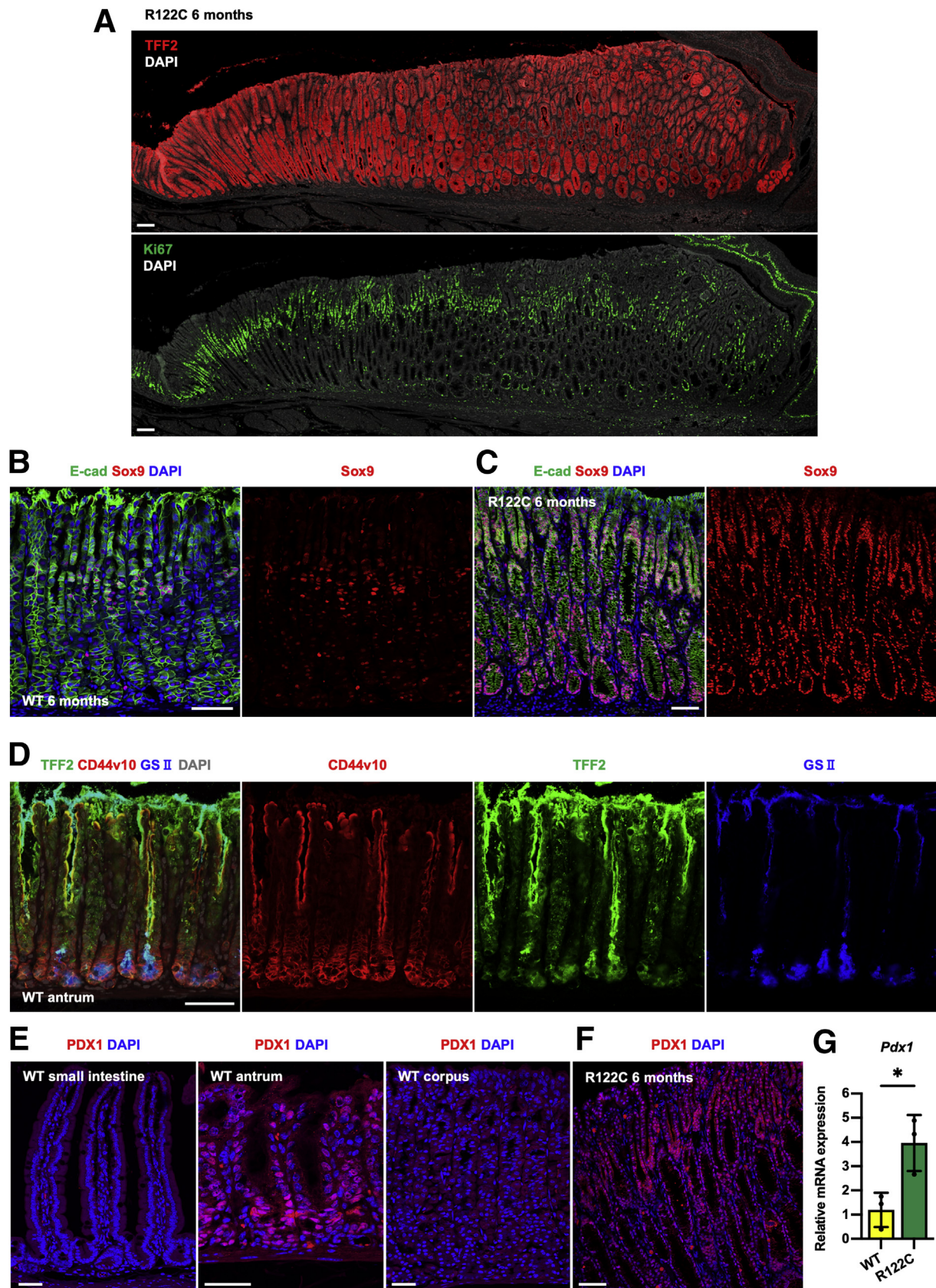
Figure 10. Characterization of metaplastic glands by using antral markers. (*A*) IF staining for Ki67 and TFF2 in the corpus of 6-month-old *RUNX3*$^{R122C/R122C}$ mice. (*B* and *C*) IF staining for E-cad and Sox9 in the corpus of 6-month-old (*B*) WT and (*C*) *RUNX3*$^{R122C/R122C}$ mice. (*D*) IF staining for TFF2, CD44v10, and GSII in the antrum of WT mice. IF staining for PDX1 in the (*E*) small intestine, antrum, and corpus of WT mice, and in the (*F*) corpus of 6-month-old *RUNX3*$^{R122C/R122C}$ mice. (*G*) qPCR for *Pdx1* expression levels in the corpus tissues of 6-month-old WT and *RUNX3*$^{R122C/R122C}$ mice (*n* = 3 mice each). *Scale bars*: 100 μm (*A*), 50 μm (*B–F*). Data are presented as the means ± SEM and were analyzed by the Student *t* test. **P* < .05. DAPI, 4',6-diamidino-2-phenylindole.
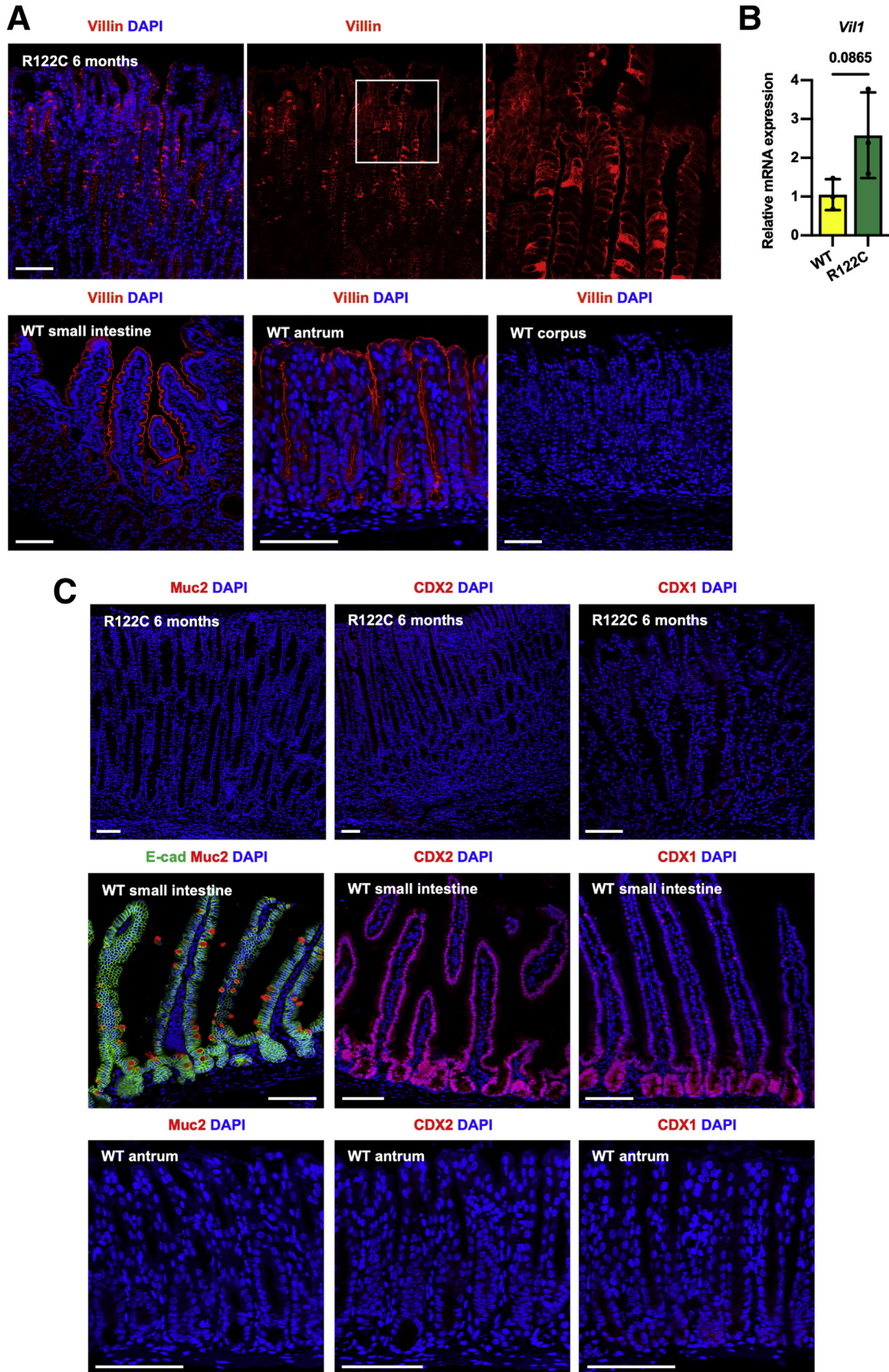
Figure 11. Characterization of metaplastic glands by using intestinal markers. (A) IF staining for villin in the corpus of 6-month-old $RUNX3^{R122C/R122C}$ mice, and in the small intestine, antrum, and corpus of WT mice. (B) qPCR for $Vil1$ expression level in the corpus tissues of 6-month-old WT and $RUNX3^{R122C/R122C}$ mice ($n = 3$ mice each). (C) IF staining for Muc2, CDX2, and CDX1 in the corpus of 6-month-old $RUNX3^{R122C/R122C}$ mice, and in the small intestine and antrum of WT mice. *Scale bars*: 100 μm. Data are presented as the means $\pm$ SEM and were analyzed by the Student t test. *Box* indicates enlarged region. DAPI, 4',6-diamidino-2-phenylindole.
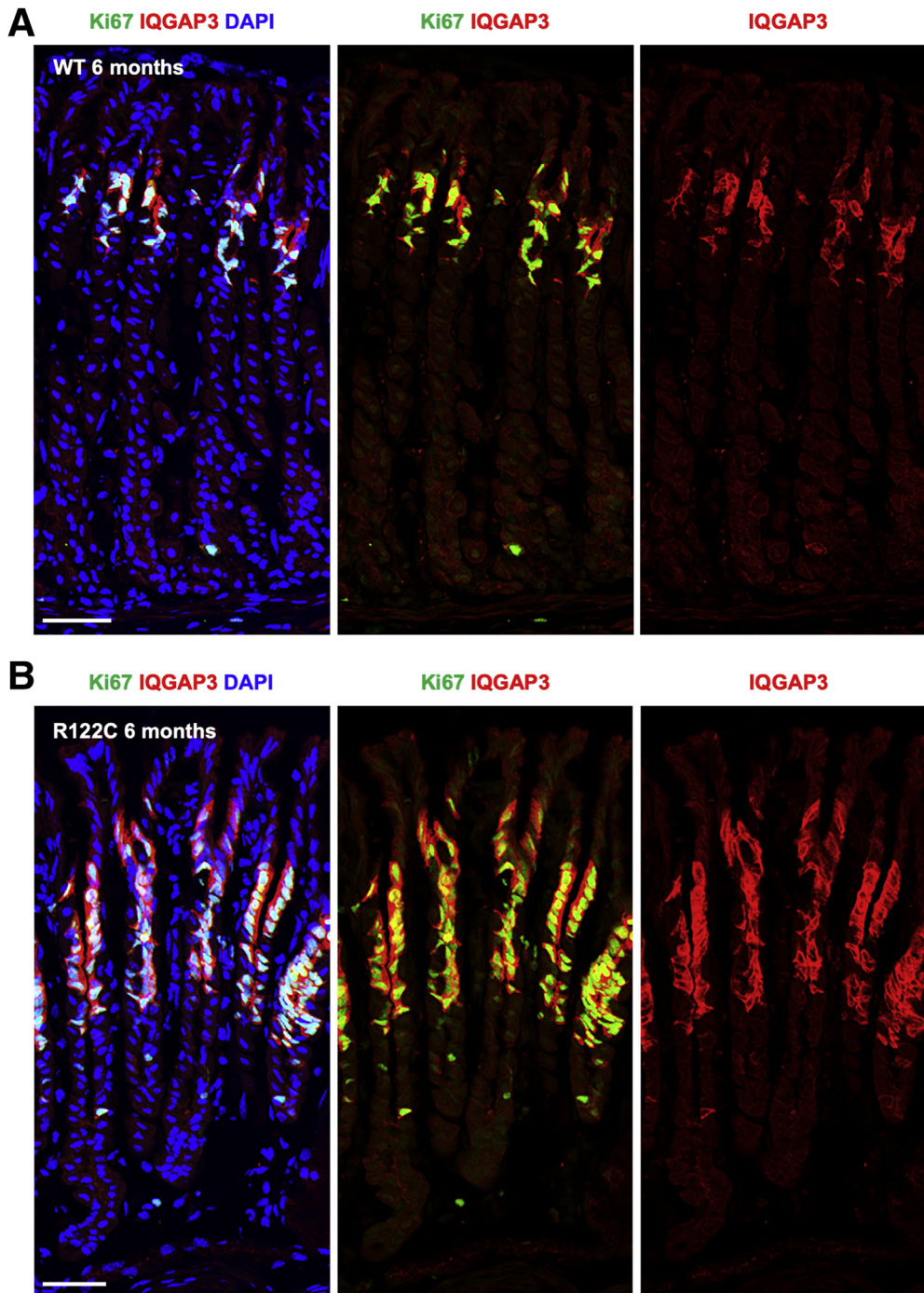
Figure 12. IQGAP3 expression in the corpus tissues of 6-month-old WT and RUNX3$^{R122C/R122C}$ mice. (*A* and *B*) IF staining for Ki67 and IQGAP3 in the corpus tissues of 6-month-old (*A*) WT and (*B*) RUNX3$^{R122C/R122C}$ mice. *Scale bars*: 100 μm. DAPI, 4′,6-diamidino-2-phenylindole.

RUNX3^{WT}) or Myc-tagged RUNX3^{R122C} (Myc- RUNX3^{R122C}), and Flag-tagged wild-type BRD2 (Flag-BRD2) into Human Embryonic Kidney cells 293 (HEK293) cells and analyzed the interaction using co-immunoprecipitation, followed by immunoblotting (IB). Although RUNX3^{WT} interacted with BRD2 at 2 hours after stimulation with 10% serum, RUNX3^{R122C} did not (Figure 16*A*). The RUNX3^{R122C} mutation abolished RUNX3-BRD2 and RUNX3-p300 interactions (1–2 h after serum stimulation), and RUNX3–cyclin D1 interaction (4–8 h after serum stimulation) (Figure 16*B*). These results show that RUNX3^{R122C} results in the deregulation of

R-point and allows unrestrained entry into the S-phase, a hallmark of cancer.

The Maturation Arrest of Progenitor Cells Occurred in the Corpus of 6-Month-Old RUNX3$^{R122C/R122C}$ Mice

Phosphorylation of the pRb is associated with passage through the R-point.[41] To assess the pRb phosphorylation status, we immunostained the corpus with antibodies
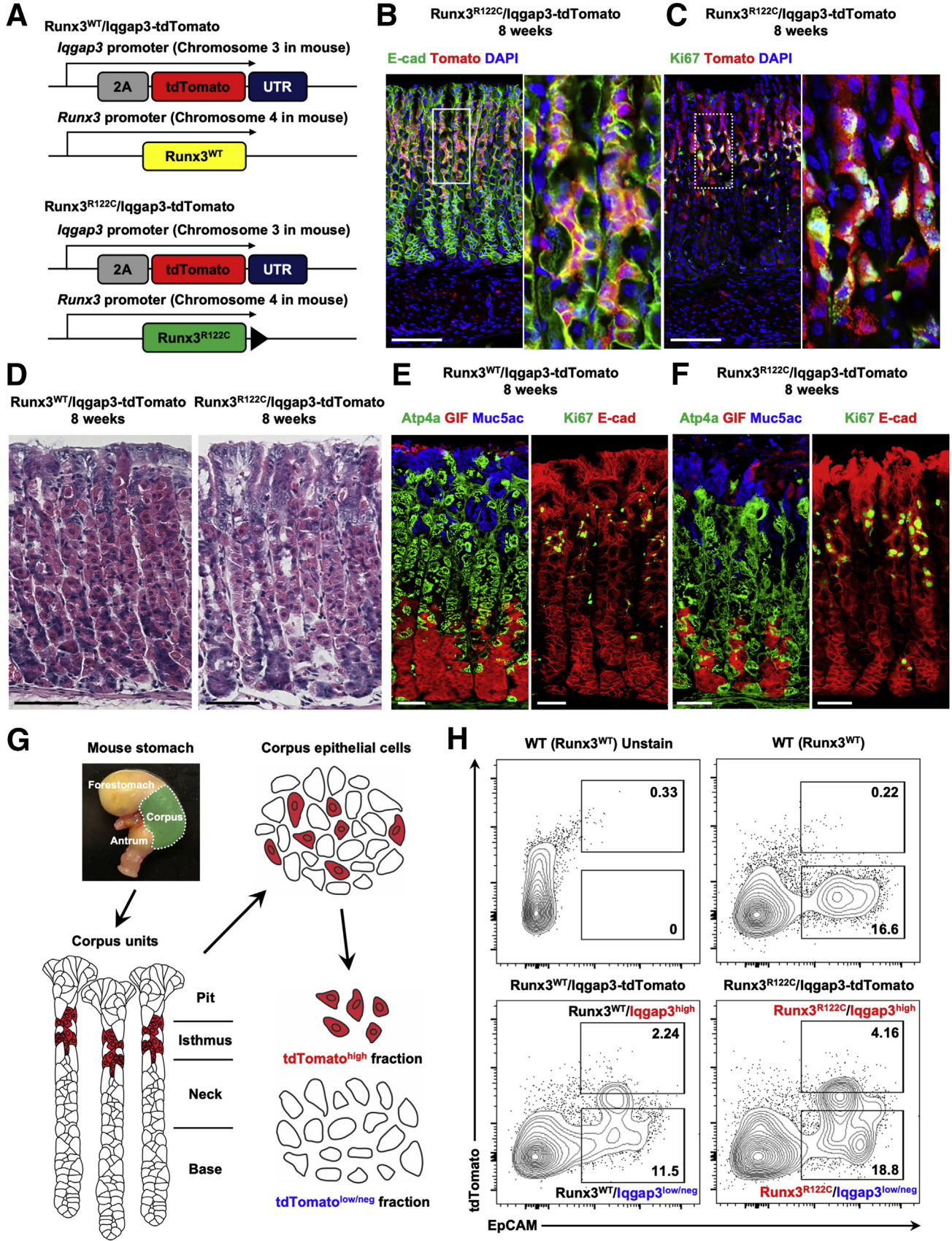
against phosphorylated pRb. The levels of phosphorylated pRb protein were increased markedly in those of 6-month-old $RUNX3^{R122C/R122C}$ mice compared with those in similar-aged WT mice (Figures 16C and 17A). Notably, the protein was highly expressed not only in the isthmus region but also in the gland base, where terminally differentiated cells reside under normal conditions. Most of the cells located below the isthmus in $RUNX3^{R122C/R122C}$ mice expressed phosphorylated pRb, suggesting that they were at the active cell-cycling phase.

Using the 30-minute labeling index as a measure of mitotic activity, high mitotic activity was observed in 3 isthmus cell types: granule-free, pre-pit, and pre-neck cells. Preparietal cells were not labeled 30 minutes after a ^{3}H-thymidine injection.[42] In general, Ki67 is present during all active phases of the cell cycle, but is absent in resting cells. DNA replication licensing factor Minichromosome maintenance complex component 2 (MCM2) is expressed not only in actively cycling cells, but also noncycling cells with proliferative capacity; MCM2 is therefore a more sensitive indicator of cells with growth potential than Ki67.[43,44]

We therefore immunostained the corpus of WT and $RUNX3^{R122C/R122C}$ mice with antibodies of Ki67 and MCM2. In the isthmus of WT mice, the distribution of MCM2 is slightly wider than that of Ki67 (Figure 17B and C). Considering these findings and the experiments of 30-minute labeling index, MCM2+Ki67- cells are likely indicative of immature pre-pit and pre-neck progenitor cells at the G_1 phase of the cell cycle. In the gland base of WT mice, MCM2 was down-regulated and degraded, indicating that the cells of the gland base entered the G_0 phase. In contrast, the difference of distribution between Ki67 and MCM2 in the isthmus of $RUNX3^{R122C/R122C}$ mice is much larger than that of WT mice (Figures 16D, upper panel, and 17B and C). This indicated that stem cells of $RUNX3^{R122C/R122C}$ mice strongly generate both pre-pit and pre-neck progenitor cells, which possess proliferative potential and can enter the cell cycle rapidly. Interestingly, Ki67+ or MCM2+ cells were detected at the gland base of $RUNX3^{R122C/R122C}$ mice (Figure 16D, lower panel). These cells potentially reflect the dedifferentiation of mature chief cells and re-entry into the cell cycle.[45,46]

Discussion

It has been proposed that RUNX3 serves as a gatekeeper linking the oncogenic Wnt and anti-oncogenic TGF-β/Bone morphogenetic proteins (BMPs) signaling pathways in intestinal tumorigenesis.[47] RUNX3 loss leads to high oncogenic Wnt activity and is a key event in the induction of a precancerous state in the stomach.[12] Chronic H $pylori$ infection inactivates RUNX3 in gastric carcinogenesis through multiple mechanisms.[48,49] The fact that RUNX3-deficiency alone is enough to induce a precancerous state in the stomach indicates that its inactivation is crucial for gastric cancer initiation.

$RUNX3^{R122C}$ was identified in a patient with gastric cancer, and the exogenous expression of $RUNX3^{R122C}$ failed to limit tumor growth in nude mice.[11] To study the underlying mechanism, we generated a mouse model harboring the $RUNX3^{R122C}$ missense mutation. The stomach of the $RUNX3^{R122C/R122C}$ mice was precancerous, with a dramatic increase of isthmus stem/progenitor cells and a drastic reduction in the terminally differentiated pit, parietal, and chief cells. Furthermore, we crossed $RUNX3^{R122C}$ mice with $Iqgap3$-$2A$-$tdTomato$ reporter mice to generate $RUNX3^{R122C/R122C}$ homozygous mice carrying $Iqgap3$-$2A$-$tdTomato$.[32] Because Iqgap3 fluorescently labeled isthmus cells, we were able to isolate isthmus and nonisthmus cells from control and $Runx3^{R122C}$;$Iqgap3$-$tdTomato$ mice through flow cytometry. Myc target genes were up-regulated in the Iqgap3-tdTomato^{high} and Iqgap3-tdTomato$^{low/neg}$ epithelial fractions of $Runx3^{R122C}$;$Iqgap3$-$tdTomato$ mice, which reflected the highly proliferative state of the isthmus stem/progenitor cells. Our studies indicate that $RUNX3^{R122C}$ mutant cells are impaired in the RUNX3–BRD2–mediated regulation of the R-point, which allows continuous S-phase re-entry. Moreover, BRD2 is central for cell differentiation (albeit not in the gastrointestinal context) and plays crucial roles in the differentiation of embryonic stem cells during mesendoderm specification and Myc-associated osteoclast differentiation.[50,51] Together with these studies, our work suggests that the inability of $RUNX3^{R122C}$ to bind BRD2 led to the 2 major phenotypes that have been linked to preneoplasia, namely, highly proliferative stem/progenitor cells and inhibition of cell differentiation.

Interestingly, $RUNX3^{R122C/R122C}$ mice showed mucous neck cell hyperplasia, reminiscent of that induced by H $pylori$ colonization of epithelial stem/progenitor cell compartments.[52] Although little is known about how H $pylori$ induces mucous neck cell hyperplasia, the induction of a similar phenotype in our $RUNX3^{R122C/R122C}$ mouse model, although not infected with H $pylori$, indicated that RUNX3

Figure 13. (*See previous page*). Sorting of the isthmus and nonisthmus cells from 8-week-old $RUNX3^{R122C/R122C}$ mice using $Iqgap3$-$2A$-$tdTomato$ mice. (A) Schematic representations of the genetic constructs used to establish the $Runx3^{WT}$/$Iqgap3$-$tdTomato$ (control) and $RUNX3^{R122C/R122C}$;$Iqgap3$-$2A$-$tdTomato$ ($Runx3^{R122C}$/$Iqgap3$-$tdTomato$) mice model. (B) IF staining for E-cad and tdTomato in the corpus of 8-week-old $Runx3^{R122C}$/$Iqgap3$-$tdTomato$ mice. (C) IF staining for Ki67 and tdTomato in the corpus of 8-week-old $Runx3^{R122C}$/$Iqgap3$-$tdTomato$ mice. (D) H&E staining in the corpus tissues of 8-week-old control and $Runx3^{R122C}$/$Iqgap3$-$tdTomato$ mice. (E) IF staining for Atp4a, GIF, Muc5ac, Ki67, and E-cad in the corpus of 8-week-old control mice. (F) IF staining for Atp4a, GIF, Muc5ac, Ki67, and E-cad in the corpus of 8-week-old $Runx3^{R122C}$/$Iqgap3$-$tdTomato$ mice. (G) Outline of the experimental strategy used. (H) Representative flow cytometry plots of the isolated tdTomato/Iqgap3-high (Iqgap3^{high}) and tdTomato/Iqgap3-low or negative (Iqgap3$^{low/neg}$) epithelial cell fractions from the corpus tissues of 8-week-old control ($Runx3^{WT}$/$Iqgap3$-$tdTomato$ mice) and $Runx3^{R122C}$/$Iqgap3$-$tdTomato$ mice ($n = 10$ mice each, at least 2 biologically independent experiments). *Scale bars*: 100 μm (B and C), 50 μm (D–F). *Boxes* indicate enlarged regions. DAPI, 4',6-diamidino-2-phenylindole; UTR, untranslated region.
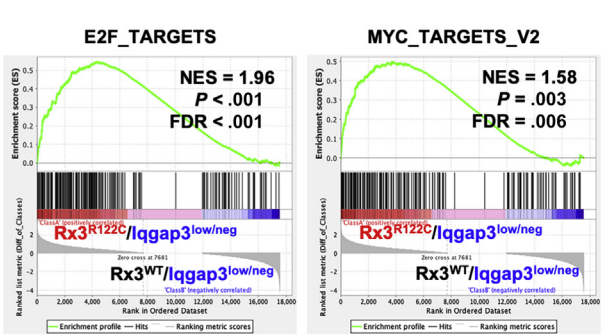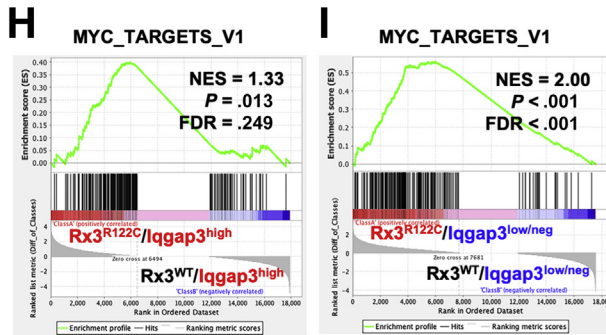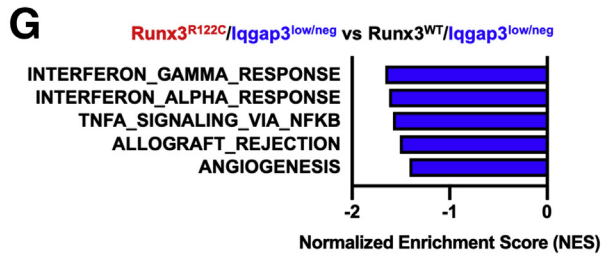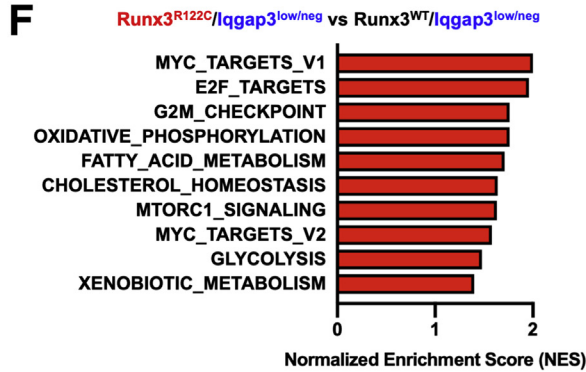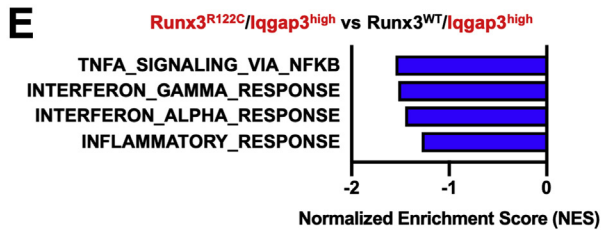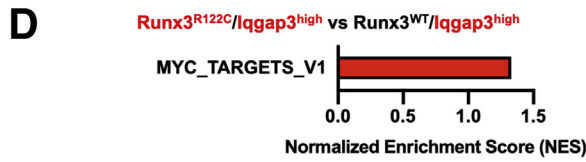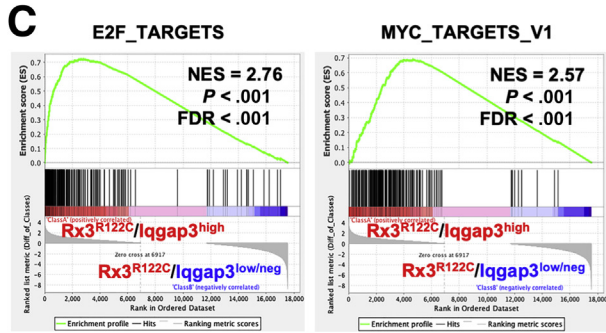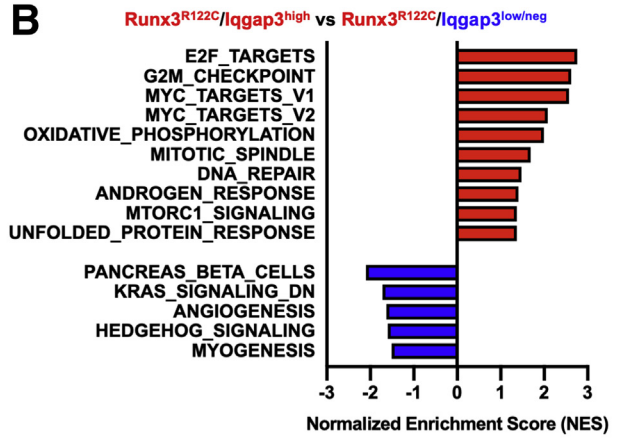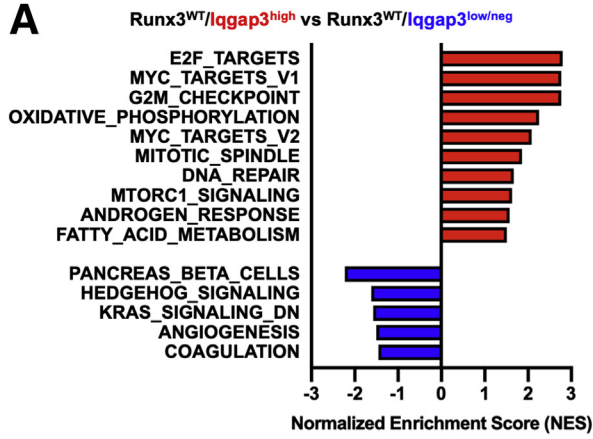
play a pivotal role. Indeed, *H pylori* infection has been associated with hypermethylation and subsequent epigenetic silencing of the *RUNX3* gene.[5]

The *RUNX3[R122C/R122C]* mice presented with precancerous lesions after 6 months. This suggests that the RUNX3[R122C]-mediated hyperproliferative state induced DNA replication stress and genomic instability, resulting in the rapid acquisition of oncogenic mutations in the differentiation-defective progenitor cells and the clonal expansion of a dominant stem-like population. We previously reported that *eR1-CreERT2:Kras[G12D/+]* and *Iqgap3-2A-CreERT2;Kras[G12D/+]* mice induced pseudopyloric metaplasia, which was characterized by a massive induction of Muc5ac+ pit cells.[32,53] These results indicate that the specific expression of hyperactivated Ras in isthmus stem cells, in which the R-point is normal, could produce mature pit cells. It follows that deregulation of the R-point in *RUNX3[R122C/R122C]* mice is associated with impaired pit cell maturation, and subsequent accumulation of isthmus stem cells. Furthermore, the corpus of *RUNX3[R122C/R122C]* mice showed substantial maturation arrest, as evidenced by reduced numbers of terminally differentiated pit, parietal, and chief cells. It is conceivable that the RUNX3[R122C] progenitor cells could not enter the irreversible G_0 phase, which is the hallmark of terminal differentiation. Similarly, the dedifferentiation of mature chief cells in the corpus of *RUNX3[R122C/R122C]* mice suggests that the inability of chief cell to maintain quiescence in the G_0 phase led to cell-cycle re-entry, thereby contributing to the pool of rapidly proliferating stem-like cells.

Our results raised profound questions on how isthmus progenitor cells exit and re-enter the S-phase and how the decision between proliferation and differentiation is made. The enhanced E2F signaling and increased expression of its downstream target MCM2 indicate that RUNX3[R122C] mutant cells, which lack a functional R-point, are poised at a proliferation-competent state with the ability to rapidly license DNA replication. Further in-depth studies on replication licensing and kinetics of G_1 phase in RUNX3[R122C] cells likely will yield insights on the determination of stem/progenitor cell fate in the corpus.

This study shows that the gastric epithelium of *RUNX3[R122C/R122C]* mice is cancer-prone, which is consistent with the notion of RUNX3 as a gatekeeper of gastric carcinogenesis. Considering that RUNX3 frequently is inactivated during early gastric carcinogenesis, understanding the relationship between gastric stem/progenitor cells and R-point decision making under RUNX3[R122C] mutation-induced precancerous conditions is essential to elucidate the initial stages of gastric tumorigenesis. Although the stomach of *RUNX3[R122C/R122C]* mice showed a precancerous state, the stomachs of *RUNX3[R122C/R122C]* mice older than 1.5 years showed no occurrence of gastric cancer. Therefore, additional alterations likely are required for the development of a full-fledged malignancy. Alternatively, RUNX3 is critical for lineage commitment of various immune cell types.[54] It is conceivable that differentiation blocks in both epithelial and immune cells, as well as their crosstalk, contributed to the unique phenotype of *RUNX3[R122C/R122C]* mice. Further studies of *RUNX3[R122C/R122C]* mice will therefore shape our understanding of stem cell-intrinsic and extrinsic mechanisms in preneoplasia.

Materials and Methods
Mice and Treatment

All mice were of the C57BL/6 inbred strain. WT mice were purchased from InVivos Pte Ltd (Singapore). The *RUNX3[R122C]* strain (accession no. CDB0966K: http://www2.clst.riken.jp/arg/mutant%20mice%20list.html) was generated at the RIKEN Centre for Biosystems Dynamics Research (Kobe, Hyogo, Japan; as described https://www.riken.jp/en/research/labs/bdr). The *Iqgap3-2A-tdTomato* reporter mice were used as described previously.[32] For all experiments, adult mice (not selected for sex) were used at a minimum age of 6–8 weeks and mice were allocated randomly to experimental groups.

During the experiments, the mice were maintained in autoclaved micro-isolator cages and provided with normal tap water and chow ad libitum in a temperature-controlled room under a 12-hour light/dark cycle. All mice were handled in strict accordance with good animal practice as defined by the Institution of Animal Care and Use Committee, and the experiments were approved by the Institutional Animal Care and Use Committee of RIKEN Kobe Branch, and the Institution of Animal Care and Use Committee and the Office of Safety, Health, and Environment at the National University of Singapore.

Figure 14. (*See previous page*). Comparison of RNA sequences obtained from the isolated isthmus and nonisthmus cells of 8-week-old control and *Runx3[R122C]/Iqgap3-tdTomato* mice. (*A*) GSEA using hallmark gene sets from the Molecular Signatures Database. *Red bars* indicate the pathways enriched in the Runx3[WT]/Iqgap3^{high} fraction and *blue bars* indicate those enriched in the Runx3[WT]/Iqgap3[low/neg] fraction. The statistically significant signatures were selected ($P < .05$; false discovery rate [FDR] < 0.05). (*B*) GSEA using hallmark gene sets. *Red bars* indicate the pathways enriched in the Runx3[R122C]/Iqgap3^{high} fraction and *blue bars* indicate those enriched in the Runx3[R122C]/Iqgap3[low/neg] fraction. The statistically significant signatures were selected ($P < .05$; FDR < 0.05). (*C*) GSEA showing enrichment of E2F targets, MYC targets, and mitotic spindle gene signatures in the Runx3[R122C]/Iqgap3^{high} fraction, and enrichment of Kras signaling down signature in the Runx3[R122C]/Iqgap3[low/neg] fraction. (*D* and *E*) GSEA using hallmark gene sets. (*D*) *Red bars* indicate the pathways enriched in the Runx3[R122C]/Iqgap3^{high} fraction and (*E*) *blue bars* indicate those enriched in the Runx3[WT]/Iqgap3^{high} fraction. The statistically significant signatures were selected ($P < .05$; FDR < 0.25). (*F* and *G*) GSEA using hallmark gene sets. (*F*) *Red bars* indicate the pathways enriched in the Runx3[R122C]/Iqgap3[low/neg] fraction and (*G*) *blue bars* indicate those enriched in the Runx3[WT]/Iqgap3[low/neg] fraction. The statistically significant signatures were selected ($P < .05$; FDR < 0.05). (*H*) GSEA showing enrichment of MYC targets V1 gene signatures in the Runx3[R122C]/Iqgap3^{high} fraction. (*I*) GSEA showing enrichment of MYC targets V1, E2F targets, and MYC targets V2 gene signatures in the Runx3[R122C]/Iqgap3[low/neg] fraction.

Runx3^R122C^/Iqgap3^high^ vs Runx3^WT^/Iqgap3^high^

A

B
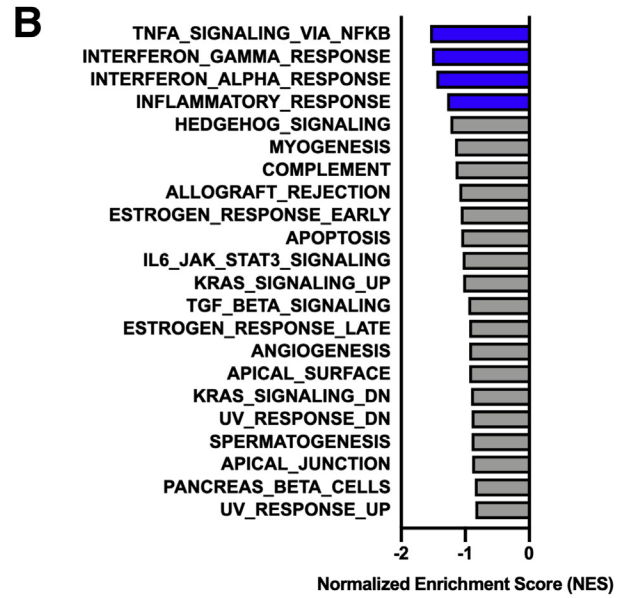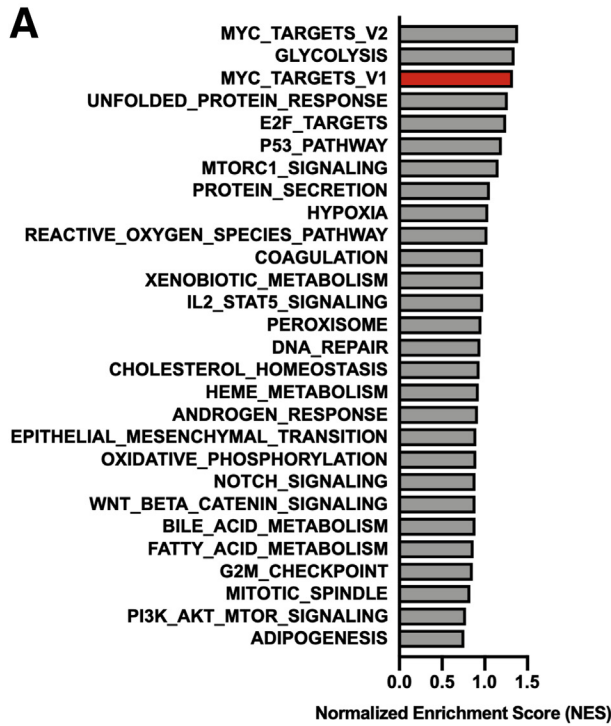
Runx3^R122C^/Iqgap3^low/neg^ vs Runx3^WT^/Iqgap3^low/neg^

C

D
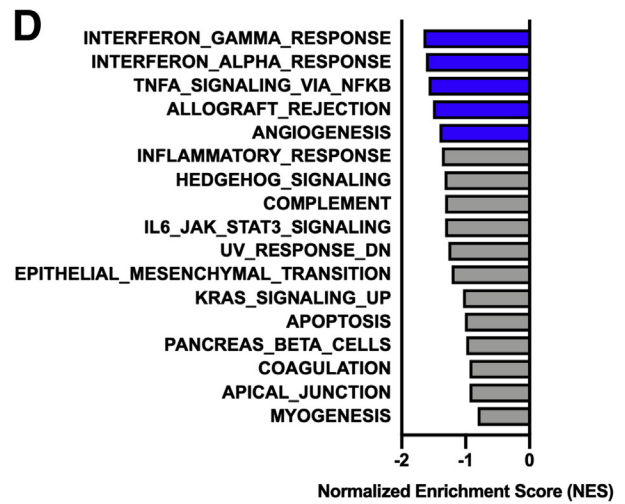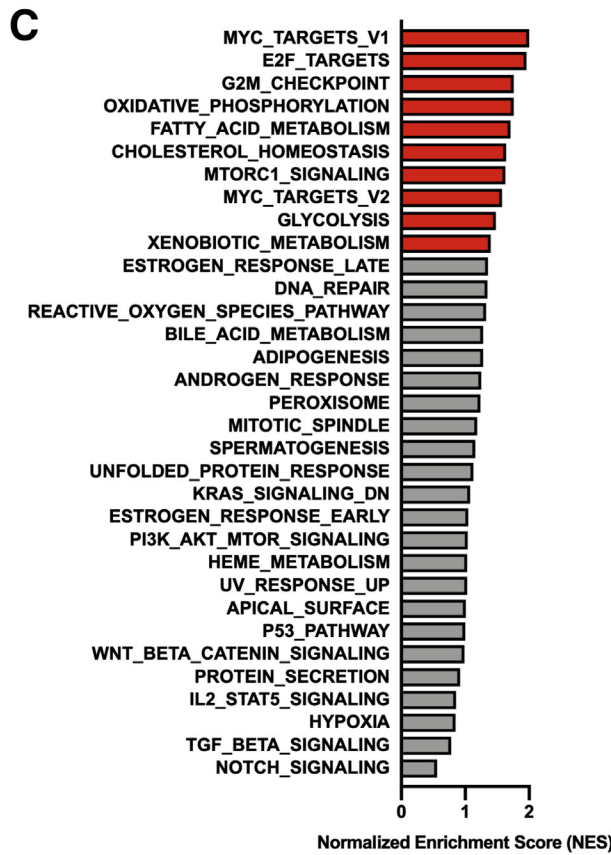
Generation of RUNX3[R122C] Knock-In Transgenic Mice

Genomic fragments encompassing exons 2–4 containing RUNX3[R122C] (arginine) were isolated from C57BL/6 BAC clones (BACPAC Resources, Oakland, CA) using high-fidelity PCR. PCR-based site-directed mutagenesis was performed to introduce a point mutation at RUNX3[R122C] in exon 3 of Runx3. A knock-in vector was generated by cloning the genomic fragments containing the intronic region in exon 3 into the polylinker of the target vector neomycin (NEO)-diphtheria toxin A (DTA) cassette containing a *Pgk-Neo* gene flanked by locus of X-over P1 (LoxP) sites and a DTA cassette (http://www2.clst.riken.jp/arg/cassettes.html) for the selection. The RUNX3[R122C] mutation was generated by homologous recombination in TT2 cells targeting the knock-in vector to the intronic region between exon 3 of Runx3.[55] The neomycin expression cassette then was excised by crossing the chimera mice with EIIa-Cre mice (003724; Jackson Laboratory, Bar Harbor, ME).[56]

Mice Genotyping

Mouse tail DNA for initial genotyping of pups was isolated using DirectPCR Lysis Reagent (Tail) (Viagen Biotech, Los Angeles, CA) containing proteinase K (Merck, Darmstadt, Germany) according to the manufacturer's instructions. PCRs were performed with GoTaq Green Master Mix (Promega, Madison, WI) by using the following primers: *R122C* forward: 5′-GGAGAGTTTTCTCGCAGGTTC-3′, reverse: 5′-GTACCTGAAGAAGCCTCCAGC-3′; *tdTomato* forward: 5′-CTGTTCCTGTACGGCATGG-3′, reverse: 5′-GGCATTAAAG-CAGCGTATCC-3′; and *Iqgap3*-intact forward: 5′-CAGCTGCAGTATGAGGGTGT-3′, reverse: 5′-GGTAATGGA-GAAGCGCAGCAGCC-3′.

For genotyping by Sanger sequencing, PCR products were amplified using TaKaRa LA Taq DNA Polymerase (Takara, Kusatsu, Japan), were treated with ExoSAP-IT (USB Corporation, Cleveland, OH), and then labeled with the BigDye Terminator Cycle Sequencing Kit v3.1 (Life Technologies, Carlsbad, CA) using the same PCR primers as in the amplification reactions. Sequencing products were loaded on an ABI3500 capillary sequencer (Life Technologies). The following primers were used for sequencing: R122C_seq forward: 5′-TGATGGCCGGCAATGATGAGAACTACTCCG-3′, reverse: 5′-GCGGCCGCAGCACCGGAGACTTCA-GAAGTTGCTAAACC-3′.

IF and Histologic Analyses

Mouse stomachs were cut longitudinally following the greater curvature. The contents of the stomachs were removed by washing with phosphate-buffered saline (PBS),

and the tissue subsequently was spread on the silicone rubber sheet using holding pins. Stomach tissues were fixed in 1% or 4% paraformaldehyde for either 2 hours at 4°C for frozen processing or overnight at 4°C for paraffin processing. For frozen sections, fixed tissues were embedded in OCT compound (Leica Biosystems, Wetzlar, Germany) after incubation with sucrose in PBS at 4°C. For paraffin sections, tissues were processed through a graded ethanol series, followed by xylene, and then embedded in paraffin. Five-micrometer paraffin-embedded tissue sections or 5-μm OCT frozen tissue sections were processed using a standard histologic protocol.

Frozen slides were thawed to room temperature and rehydrated, whereas paraffin slides were deparaffinized, rehydrated through graded alcohols to deionized water, and subjected to antigen retrieval (Agilent Technologies, Santa Clara, CA) in a pressure cooker (100°C) for 20 minutes.

To stain paraffin or frozen tissue slides, blocking was performed with Dako (Carpinteria, CA) protein block (Agilent Technologies), 3% bovine serum albumin (Merck) in TBST, 5% goat serum (Merck) in TBST, or 5% skimmed milk in Tris buffered saline with Tween-20 (TBST). The primary antibodies were diluted in the blocking reagent and incubated with the tissue slides overnight at 4°C. Slides were washed in TBST and incubated with Alexa-Fluor–conjugated secondary antibodies diluted in 5% skimmed milk in TBST for 1 hour at room temperature. 4′,6-Diamidino-2-phenylindole was used to counterstain nuclei in the indicated experiments, and the sections were mounted in ProLong Diamond Antifade Mountant (Thermo Fisher Scientific, Waltham, MA). Stained sections were visualized using a Nikon A1R confocal laser scanning microscope system attached to an Eclipse Ti (Nikon, Tokyo Japan) microscope or Zeiss LSM880 with Airyscan (Zeiss, Oberkochen, Germany)) microscope. IF images were analyzed and post-imaging adjustments were performed with Adobe Photoshop CC (Adobe, San Jose CA). The primary and secondary antibodies used in this study are listed later.

H&E and periodic acid–Schiff staining procedures were performed according to standard protocols. The images were captured using TissueFAXS PLUS (TissueGnostics, Vienna, Austria) coupled onto an Eclipse Ti (Nikon) microscope.

Antibodies Used for IF Staining

Paraffin and frozen tissue sections were stained with the following primary antibodies: rat anti-CD45 (1:500, 14-0451-82; eBioscience, San Diego, CA), rat anti–E-cadherin (1:500, ab11512; Abcam, Cambridge, UK), mouse anti–E-cadherin Alexa Fluor 488/555/647 conjugate (1:200, 560061/560064/560062; BD Biosciences, San Jose, CA),

Figure 15. (*See previous page*). Enriched biological pathways from GSEA hallmark gene sets of Iqgap3^{high} or Iqgap3[low/neg] fractions of 8-week-old control and *Runx3[R122C]/Iqgap3-tdTomato* mice. (*A* and *B*) GSEA using hallmark gene sets from the Molecular Signatures Database. (*A*) *Red bars* indicate the pathways enriched in the Runx3[R122C]/Iqgap3^{high} fraction and (*B*) *blue bars* indicate those enriched in the Runx3[WT]/Iqgap3^{high} fraction. The statistically significant signatures were selected ($P < .05$; false discovery rate < 0.25). (*C*) *Red bars* indicate the pathways enriched in the Runx3[R122C]/Iqgap3[low/neg] fraction and (*D*) *blue bars* indicate those enriched in the Runx3[WT]/Iqgap3[low/neg] fraction. The statistically significant signatures were selected ($P < .05$; false discovery rate < 0.05).
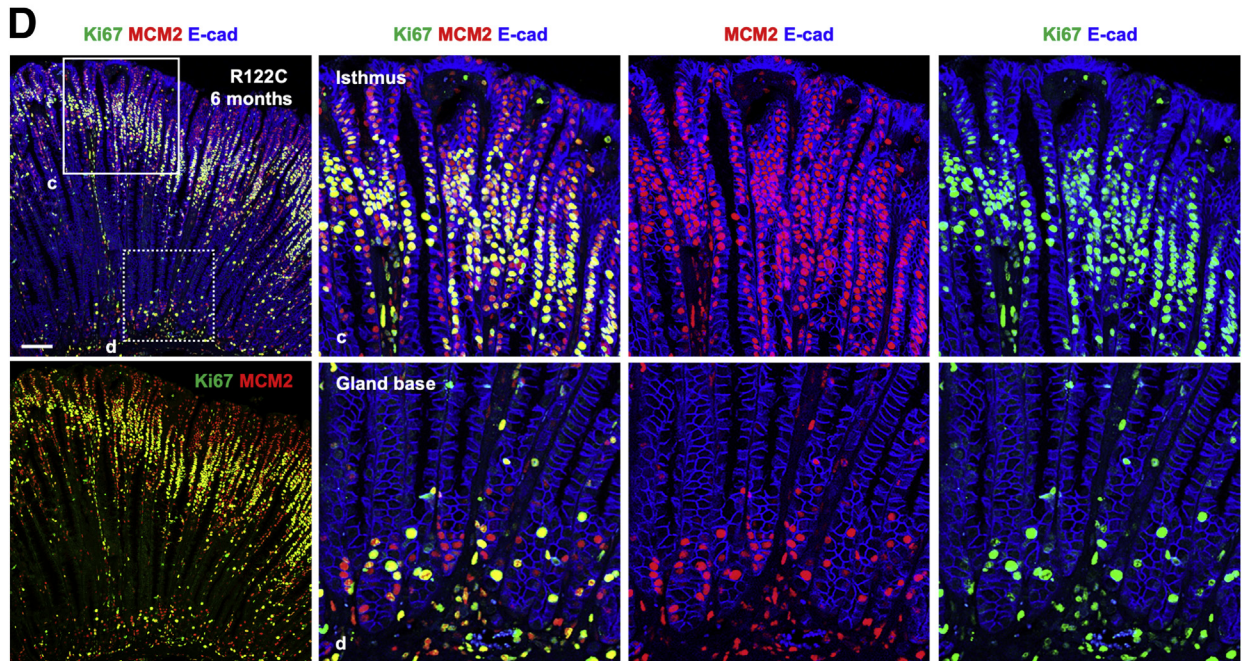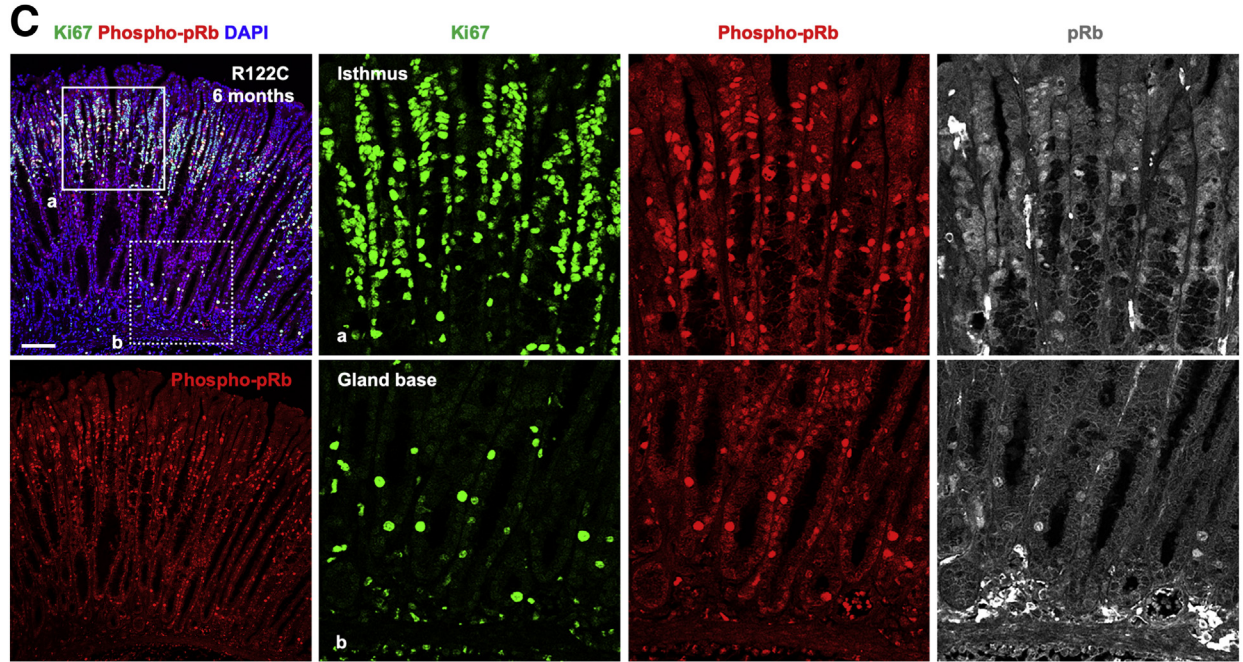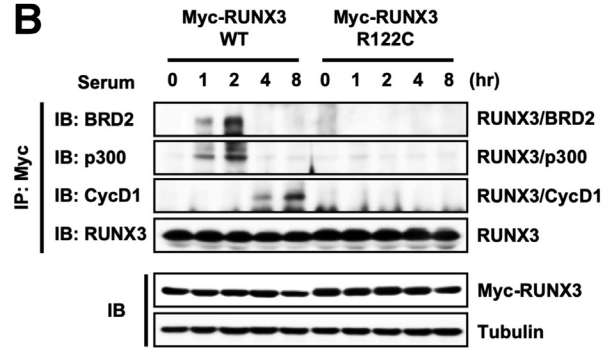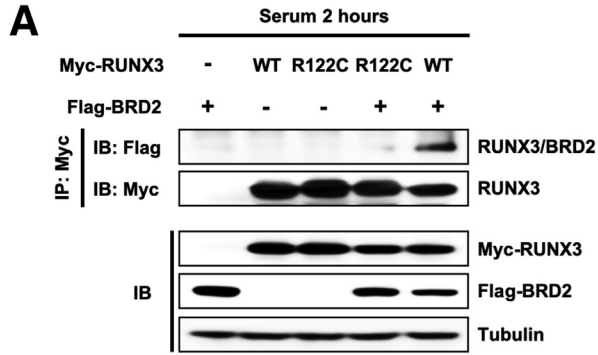
mouse anti–H,K-ATPase α subunit (1:1000, D031-3; MBL International, Woburn, MA), anti-lectin GSII Alexa Fluor 488/647 conjugate (1:1000, L-21415/L-32451; Molecular Probes, Eugene, OR), rabbit anti-GIF (1:2000, provided by D.H. Alpers, Washington University School of Medicine, St. Louis, MO), goat anti-Muc5ac (1:200, sc-16903; Santa Cruz Biotechnology, Santa Cruz, CA), goat anti– chromogranin A (1:500, sc-1488; Santa Cruz Biotechnology), rat anti-Ki67 (1:1000, 14-5698-82; Thermo Fisher Scientific), rabbit anti-TFF2 (1:100, 13681-1-AP; Proteintech, Rosemont, IL), rabbit anti-Sox9 (1:1000, AB5535; Merck Millipore), rat anti-CD44v10 (1:500, LKG-M002; Cosmo Bio, Tokyo, Japan), rabbit anti-PDX1 (1:200, ab47267; Abcam), rabbit anti-Red fluorescent protein (1:500, PM005; MBL International), mouse anti-pRb (1:200, sc-102; Santa Cruz Biotechnology), rabbit anti–phospho-pRb (1:200, 8516; Cell Signaling Technology, Danvers, MA), rabbit anti-MCM2 (1:400, 3619; Cell Signaling Technology), rat anti-CD68 (1:200, MA5-16674; Thermo Fisher Scientific), rat anti-F4/80 (1:200, MCA497; Bio-Rad, Hercules, CA), rabbit anti-CD163 (1:100, ab182422; Abcam), rabbit anti–villin (1:100, ab130751; Abcam), rabbit anti-Muc2 (1:500, sc-15334; Santa Cruz Biotechnology), rabbit anti-CDX2 (1:100, MA5-14494; Thermo Fisher Scientific), rabbit anti-CDX1 (1:200, NBP1-49538; Novus Biologicals, Centennial, CO), rabbit anti-IQGAP3 (1:200, provided by Sachiko Tsukita, Osaka University, Osaka, Japan). The peroxidase-conjugated secondary antibodies were anti-goat/mouse/rabbit/rat Alexa 488/546/555/633/647 IgG (1:200; Invitrogen, Carlsbad, CA) for IF. Immunostaining experiments were repeated on at least 3 tissue sections per tissue block.

Single-Molecule RNA ISH

Tissues were fixed in 10% formalin for 24 hours, embedded in paraffin, and cut into 5-μm sections. ISH was performed using the RNAscope 2.5 HD Reagent Kit (Advanced Cell Diagnostics, Hayward, CA) according to the manufacturer's instructions. Probes for ISH designed and manufactured by a commercial company (Advanced Cell Diagnostics, Hayward, CA) were as follows: *Runx3* (451271), *Cdh1* (408651-C2), *Ptprc* (318651-C2), *Acta2* (319531-C2), *Mki67* (416771-C2), Duplex-positive control (321651), and negative control (320751). Images were acquired by TissueFAXS (TissueGnostics).

Gland Isolation, Cell Dissociation, and Organoid Culture

After dissection, mouse stomachs were opened up longitudinally along the greater curvature and washed several times with ice-cold Dulbecco's PBS without magnesium and calcium (DPBS without Ca^{2+}/Mg^{2+}). The stomach was laid flat, and the forestomach and antrum were removed carefully. The remaining corpus was chopped into approximately 2-mm^2 pieces. The tissue was incubated in DPBS supplemented with 5 mmol/L EDTA (Sigma, St. Louis, MO), with gentle rocking at 4°C for 2 hours. The gastric units were released by vigorous shaking in cold dissociation buffer, which consisted of 54.8 mmol/L D-sorbitol and 44 mmol/L sucrose solutions prepared in DPBS. The tube was centrifuged at 150 $\times$ g for 3 minutes, the supernatant was gently removed, and the pellet was resuspended in Advanced Dulbecco's modified Eagle medium/F12 (Advanced DMEM/F-12; Thermo Fisher Scientific). After counting the number of isolated glands, 500 glands/well were embedded in ice-cold Matrigel (Corning Life Sciences, Tewksbury, MA). Suspended glands in Matrigel were plated on 24-well plates (Thermo Fisher Scientific). Matrigel polymerization was achieved by incubating the plates and slides at 37°C for 15 minutes.

Glands suspended in Matrigel then were overlaid with gastric culture medium (Advanced DMEM/F-12 supplemented with 10 mmol/L HEPES [Thermo Fisher Scientific], 1 $\times$ GlutaMAX [Thermo Fisher Scientific], 1% penicillin/streptomycin [Thermo Fisher Scientific], 1 $\times$ N2 [Thermo Fisher Scientific], 1 $\times$ B27 [Thermo Fisher Scientific], 1 mmol/L N-acetylcysteine [Merck], and 1% bovine serum albumin). The cells also were cultured with growth factors such as 100 ng/mL Noggin (Miltenyi Biotec, Auburn, CA), 50 ng/mL epidermal growth factor (Merck), 100 ng/mL fibroblast growth factor 10 (Peprotech, Rocky Hill, NJ), 10 nmol/L gastrin I (Merck), and 10 μmol/L Y-27632 (Miltenyi Biotec, initial 4 days only), R-spondin 1–conditioned medium, and WNT3A-conditioned medium. The medium supplemented with growth factors was replaced every 3–4 days. The efficiency of organoid formation was measured, and organoids were photographed and counted at 7 days post-plating. The size of organoids was measured using ImageJ software (National Institutes of Health, Bethesda, MD). Images of gastric organoids were acquired using an Eclipse TS100 (Nikon) microscope.

Flow Cytometry

Isolated mouse gastric units were incubated in TrypLE Express (Thermo Fisher Scientific) with Y-27632 (Merck) for 12 minutes at 37°C with repetitive pipetting for digestion into single cells. The cells were passed through a 30-μm cell strainer (Miltenyi Biotech) and labeled with antibodies in Hank's balanced salt solution with 2% fetal bovine serum. An anti-EpCAM APC/Cy7-conjugated antibody (118218;

Figure 16. (*See previous page*). **Dysregulation of the cell-cycle restriction point in 6-month-old *RUNX3^R122C/R122C* mice.** (*A*) HEK293 cells were transfected with Myc-RUNX3^WT or Myc-RUNX3^R122, and Flag-BRD2. Cells were serum-starved for 24 hours and then stimulated with 10% serum. Cells were harvested 2 hours later, and the protein–protein interactions were measured by immunoprecipitation (IP) and IB. (*B*) HEK293 cells were transfected with Myc-RUNX3^WT or Myc-RUNX3^R122. Cells were harvested at the indicated time points, and the levels of the indicated proteins and their time-dependent interactions were measured by IP and IB. (*C*) IF staining for Ki67, phospho-retinoblastoma protein (phospho-pRb), and total pRb in the corpus of 6-month-old *RUNX3^R122C/R122C* mice. (*D*) IF staining for Ki67, MCM2, and E-cad in the corpus of 6-month-old *RUNX3^R122C/R122C* mice. *Scale bars*: 100 μm. *Boxes* indicate enlarged regions. DAPI, 4',6-diamidino-2-phenylindole.
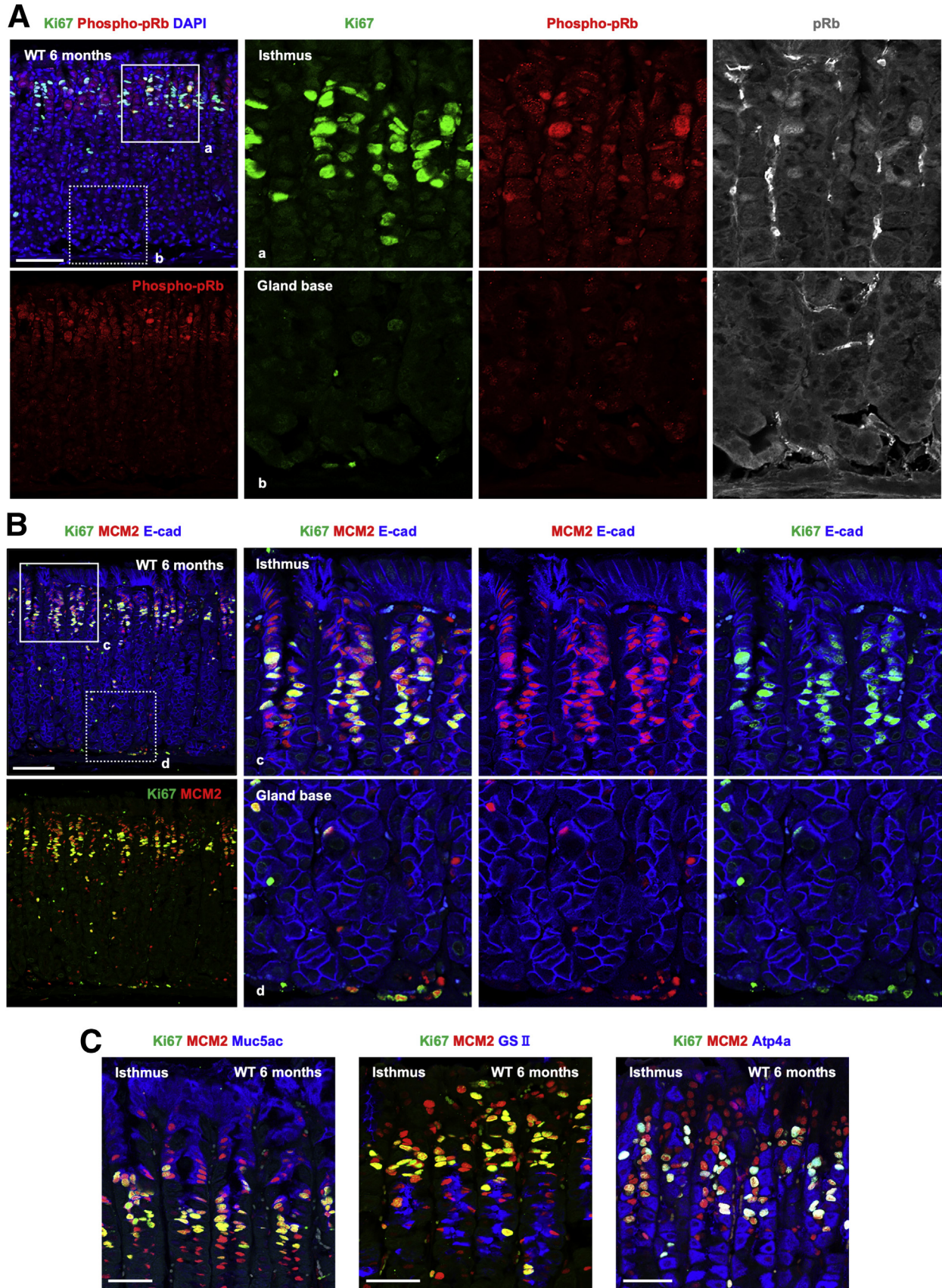
Figure 17. IF staining for phospho-pRb, total pRb, and MCM2 in the corpus of WT mice. (*A*) IF staining for Ki67, phospho-pRb, and total pRb in the corpus of 6-month-old WT mice. (*B*) IF staining for Ki67, MCM2, and E-cad in the corpus of 6-month-old WT mice. (*C*) IF staining for Ki67, MCM2, Muc5ac, GSII, and Atp4a in the isthmus region of the corpus of 6-month-old WT mice. *Scale bars*: 100 μm (*A* and *B*), 50 μm (*C*). *Boxes* indicate enlarged regions. DAPI, 4',6-diamidino-2-phenylindole.

BioLegend, San Diego, CA) was used for flow cytometry. Dead cells were excluded by 4',6-diamidino-2-phenylindole staining, and labeled cells were sorted using FACSAria II (BD Biosciences). Data were analyzed with FlowJo 10.6 (BD Biosciences).

RNA Isolation, Complementary DNA Preparation, and qPCR

Total tissue RNA was isolated using the RNeasy Mini Kit (QIAGEN, Hilden, Germany) with DNase digestion according to the manufacturer's protocol. Complementary DNA was synthesized using the PrimeScript RT Master Mix Perfect Real Time kit (TaKaRa). RNA in fluorescence-activated cell sorted cells was extracted using NucleoSpin RNA XS (MACHEREY-NAGEL, Allentown, PA) by following the manufacturer's manual. qPCR was performed in triplicate for each sample by using iTaq Universal SYBR Green Supermix (Bio-Rad) on a QuantStudio 3 PCR system (Thermo Fisher Scientific) according to the manufacturer's instructions.

The PCR program was as follows: 3 minutes at 95°C; followed by 40 cycles of 3 seconds at 95°C/30 seconds at 60°C. Relative quantification of gene expression was analyzed with QuantStudio Design and Analysis Software using the delta-delta Ct method with glyceraldehyde 3-phosphate dehydrogenase (*Gapdh*) as endogenous reference. Significance values were calculated using the Student *t* test with a *P* value cut-off of less than .05.

Primers for mouse tissue used for this study were as follows: *Muc6* forward: 5'-TGCATGCTCAATGGTATGGT-3', reverse: 5'-TGTGGGCTCTGGAGAAGAGT-3'; *Atp4a* forward: 5'-AACTTGGAGTTCGCTGTTGC-3', reverse: 5'-GGGCTGGGAATCGAGTACAT-3'; *Gif* forward: 5'-CCTGGGGCCTTATTGTCTCTTC-3', reverse: 5'-TGAAGTTGGCTGTGATGTGC-3'; *Il6* forward: 5'-TAGTCCTTCCTACCCCAATTTCC-3', reverse: 5'-TTGGTCCTTAGCCACTCCTTC-3'; *Tnf* forward: 5'-CCTGTAGCCCACGTCGTAG-3', reverse: 5'-GGGAGTAGACAAGGTACAACCC-3'; *Tff2* forward: 5'-ACCCGGGCATCAGTCCCGA-3', reverse: 5'-GCAGCTCCCAGGGAACGGGT-3'; *Cd44* forward: 5'-TCTGCCATCTAGCACTAAGAGC-3', reverse: 5'-GTCTGGGTATTGAAAGGTGTAGC-3'; *Gkn3* forward: 5'-CACTAGCGACAGTTATCCTCTGG-3', reverse: 5'-CCATTCACTCTGAACGCTGTT-3'; *Muc5ac* forward: 5'-CTGTGACATTATCCCATAAGCCC-3', reverse: 5'-AAGGGGTATAGCTGGCCTGA-3'; *Chga* forward: 5'-TCTGCCGTCTGAAGGGAAG-3', reverse: 5'-TCCTGCTTATGTTCCAGCTCC-3'; *Il-1b* forward: 5'-GCAACTGTTCCTGAACTCAACT-3', reverse: 5'-ATCTTTTGGGGTCCGTCAACT-3'; *Ptgs2* forward: 5'-TGAGCAACTATTCCAAACCAGC-3', reverse: 5'-GCACGTAGTCTTCGATCACTATC-3'; *Pdx1* forward: 5'- CCCCAGTTTACAAGCTCGCT-3', reverse: 5'-CTCGGTTCCATTCGGGAAAGG-3'; *Vil1* forward: 5'-TCAAAGGCTCTCTCAACATCAC-3', reverse: 5'-AGCAGTCACCATCGAAGAAGC-3'; and *Gapdh* forward: 5'-TTCACCACCATGGAGAAGGC-3', reverse: 5'-GGCATGGACTGTGGTCATGA-3'.

Cell Lines

HEK293 cells (ATCC) were maintained in DMEM (Gibco BRL, Grand Island, NY; Thermo Fisher Scientific) supplemented with 10% fetal bovine serum (Gibco BRL), and 1% penicillin/streptomycin. All cell lines were incubated at 37°C with 5% CO_2.

DNA Transfection, Immunoprecipitation, and IB

Transient transfections in all cell lines were performed using Lipofectamine Plus reagent and Lipofectamine (Invitrogen). Cell lysates were incubated with the appropriate monoclonal or polyclonal antibodies (2 μg antibody/500 μg lysate sample) for 3 hours at 4°C, and then with protein G–Sepharose beads (Amersham Pharmacia Biotech, Piscataway, NJ) for 1 hour at 4°C. For the detection of endogenous proteins, the lysates were incubated with the appropriate monoclonal or polyclonal antibodies (dilution range, 1:1000–1:3000) for 6–12 hours at 4°C, and then with protein G–Sepharose beads (Amersham Pharmacia Biotech) for 3 hours at 4°C. The immunoprecipitates were resolved on sodium dodecyl sulfate–polyacrylamide gel electrophoresis gels and transferred to a polyvinylidene difluoride membrane (Millipore, Billerica, MA). The membrane was immunoblotted with the appropriate antibodies after blocking, and visualized on an Amersham Imager 600 (GE Healthcare, Chicago, IL) after treatment with ECL solution (Amersham Pharmacia Biotech).

Antibodies Used for Immunoprecipitation and IB

Antibodies targeting cyclin D1 (1:1000, sc-20044; Santa Cruz Biotechnology), p300 (1:1000, sc-584; Santa Cruz Biotechnology), RUNX3 (1:3000, ab40278; Abcam), Flag (1:3000, F1804; Sigma), Myc (1:1000, sc-40; Santa Cruz Biotechnology), BRD2 (1:1000, H00006046-M01; Abnova, Taiwan), and tubulin (Lab Frontier, Koriyama, Japan) were used for IB and immunoprecipitation.

RNA-Seq and Data Analysis

RNA extracted from fluorescence-activated cell sorted IQGAP3^{high} and IQGAP3[low/neg] cells of *Runx3[WT]*; *Iqgap3-Tomato* and *Runx3[R122C]*; *Iqgap3-Tomato* mice were sent to the Beijing Genomics Institute for PCR amplification, transcriptome library preparation, and sequencing. Raw reads were aligned to mouse reference genome version GRCm38 gencode M23 (downloaded from https://www.gencodegenes.org) using STAR aligner version 2.7.1a with default parameters.[57] Read counts per gene were generated using the featureCounts function in the subread package version 2.0.0.[58] Counts per million (cpm) values were calculated using cpm function of the edgeR R package.[59] RNA extracted from the corpus tissue was sent to the Beijing Genomics Institute for transcriptome library preparation and sequencing. Sequenced reads were aligned with the STAR software to mm10, and mapped counts were used to generate the raw expression counts using the featureCounts with GENCODE transcriptome annotation. The raw expression counts then were normalized further using the cross-correlation method.[60] Normalized gene expression data were subjected to Gene Set Enrichment Analysis (GSEA) using the Broad Institute GSEA tool (http://software.broadinstitute.org/gsea/index.jsp) with the Molecular

Signatures Database v7.2 to identify enriched gene sets/pathways.

Statistical Analysis

Statistical evaluation and preparation of graphs were performed using GraphPad Prism 9 (GraphPad Software, San Diego, CA). Data are presented as the means ± SEM. Significance of intergroup differences was calculated by using the 2-tailed Student t test.

Data Availability

RNA-seq data sets generated in this study have been deposited in the Gene Expression Omnibus database under accession codes GSE190081 and GSE190506. All other supporting data are available from the corresponding authors on reasonable request.

References

1. Correa P, Houghton J. Carcinogenesis of Helicobacter pylori. Gastroenterology 2007;133:659–672.

2. Amieva M, Peek RM Jr. Pathobiology of Helicobacter pylori-induced gastric cancer. Gastroenterology 2016; 150:64–78.

3. Cancer Genome Atlas Research Network. Comprehensive molecular characterization of gastric adenocarcinoma. Nature 2014;513:202–209.

4. Maekita T, Nakazawa K, Mihara M, Nakajima T, Yanaoka K, Iguchi M, Arii K, Kaneda A, Tsukamoto T, Tatematsu M, Tamura G, Saito D, Sugimura T, Ichinose M, Ushijima T. High levels of aberrant DNA methylation in Helicobacter pylori-infected gastric mucosae and its possible association with gastric cancer risk. Clin Cancer Res 2006;12:989–995.

5. Lu XX, Yu JL, Ying LS, Han J, Wang S, Yu QM, Wang XB, Fang XH, Ling ZQ. Stepwise cumulation of RUNX3 methylation mediated by Helicobacter pylori infection contributes to gastric carcinoma progression. Cancer 2012;118:5507–5517.

6. Kim TY, Lee HJ, Hwang KS, Lee M, Kim JW, Bang YJ, Kang GH. Methylation of RUNX3 in various types of human cancers and premalignant stages of gastric carcinoma. Lab Invest 2004;84:479–484.

7. Ito Y, Bae SC, Chuang LS. The RUNX family: developmental regulators in cancer. Nat Rev Cancer 2015; 15:81–95.

8. Della Gatta G, Palomero T, Perez-Garcia A, Ambesi-Impiombato A, Bansal M, Carpenter ZW, De Keersmaecker K, Sole X, Xu L, Paietta E, Racevskis J, Wiernik PH, Rowe JM, Meijerink JP, Califano A, Ferrando AA. Reverse engineering of TLX oncogenic transcriptional networks identifies RUNX1 as tumor suppressor in T-ALL. Nat Med 2012;18:436–440.

9. Martin JW, Zielenska M, Stein GS, van Wijnen AJ, Squire JA. The role of RUNX2 in osteosarcoma oncogenesis. Sarcoma 2011;2011:282745.

10. Chuang LS, Ito K, Ito Y. RUNX family: regulation and diversification of roles through interacting proteins. Int J Cancer 2013;132:1260–1271.

11. Li Q-L, Ito K, Sakakura C, Fukamachi H, Inoue K-i, Chi X-Z, Lee K-Y, Nomura S, Lee C-W, Han S-B, Kim H-M, Kim W-J, Yamamoto H, Yamashita N, Yano T, Ikeda T, Itohara S, Inazawa J, Abe T, Hagiwara A, Yamagishi H, Ooe A, Kaneda A, Sugimura T, Ushijima T, Bae S-C, Ito Y. Causal relationship between the loss of RUNX3 expression and gastric cancer. Cell 2002;109:113–124.

12. Ito K, Chuang LS, Ito T, Chang TL, Fukamachi H, Salto-Tellez M, Ito Y. Loss of Runx3 is a key event in inducing precancerous state of the stomach. Gastroenterology 2011;140:1536–1546 e8.

13. Chuang LS, Ito Y. RUNX3 is multifunctional in carcinogenesis of multiple solid tumors. Oncogene 2010; 29:2605–2615.

14. Chi XZ, Yang JO, Lee KY, Ito K, Sakakura C, Li QL, Kim HR, Cha EJ, Lee YH, Kaneda A, Ushijima T, Kim WJ, Ito Y, Bae SC. RUNX3 suppresses gastric epithelial cell growth by inducing $p21^{WAF1/Cip1}$ expression in cooperation with transforming growth factor β-activated SMAD. Mol Cell Biol 2005;25:8097–8107.

15. Yano T, Ito K, Fukamachi H, Chi XZ, Wee HJ, Inoue K, Ida H, Bouillet P, Strasser A, Bae SC, Ito Y. The RUNX3 tumor suppressor upregulates Bim in gastric epithelial cells undergoing transforming growth factor beta-induced apoptosis. Mol Cell Biol 2006;26:4474–4488.

16. Ito K, Lim AC, Salto-Tellez M, Motoda L, Osato M, Chuang LS, Lee CW, Voon DC, Koo JK, Wang H, Fukamachi H, Ito Y. RUNX3 attenuates beta-catenin/T cell factors in intestinal tumorigenesis. Cancer Cell 2008;14:226–237.

17. Qiao Y, Lin SJ, Chen Y, Voon DC, Zhu F, Chuang LS, Wang T, Tan P, Lee SC, Yeoh KG, Sudol M, Ito Y. RUNX3 is a novel negative regulator of oncogenic TEAD-YAP complex in gastric cancer. Oncogene 2016; 35:2664–2674.

18. Ogawa S, Satake M, Ikuta K. Physical and functional interactions between STAT5 and Runx transcription factors. J Biochem 2008;143:695–709.

19. Lee YS, Lee JW, Jang JW, Chi XZ, Kim JH, Li YH, Kim MK, Kim DM, Choi BS, Kim EG, Chung JH, Lee OJ, Lee YM, Suh JW, Chuang LS, Ito Y, Bae SC. Runx3 inactivation is a crucial early event in the development of lung adenocarcinoma. Cancer Cell 2013;24:603–616.

20. Petersen CP, Weis VG, Nam KT, Sousa JF, Fingleton B, Goldenring JR. Macrophages promote progression of spasmolytic polypeptide-expressing metaplasia after acute loss of parietal cells. Gastroenterology 2014; 146:1727–1738 e8.

21. De Salvo C, Pastorelli L, Petersen CP, Butto LF, Buela KA, Omenetti S, Locovei SA, Ray S, Friedman HR, Duijser J, Xin W, Osme A, Cominelli F, Mahabeleshwar GH, Mills JC, Goldenring JR, Pizarro TT. Interleukin 33 triggers early eosinophil-dependent events leading to metaplasia in a chronic model of gastritis-prone mice. Gastroenterology 2021;160:302–316 e7.

22. Oshima M, Oshima H, Matsunaga A, Taketo MM. Hyperplastic gastric tumors with spasmolytic polypeptide-expressing metaplasia caused by tumor necrosis factor-alpha-dependent inflammation in

cyclooxygenase-2/microsomal prostaglandin E synthase-1 transgenic mice. Cancer Res 2005; 65:9147–9151.

23. Judd LM, Alderman BM, Howlett M, Shulkes A, Dow C, Moverley J, Grail D, Jenkins BJ, Ernst M, Giraud AS. Gastric cancer development in mice lacking the SHP2 binding site on the IL-6 family co-receptor gp130. Gastroenterology 2004;126:196–207.

24. Bockerstett KA, Lewis SA, Noto CN, Ford EL, Saenz JB, Jackson NM, Ahn TH, Mills JC, DiPaolo RJ. Single-cell transcriptional analyses identify lineage-specific epithelial responses to inflammation and metaplastic development in the gastric corpus. Gastroenterology 2020; 159:2116–2129 e4.

25. Naik S, Larsen SB, Cowley CJ, Fuchs E. Two to tango: dialog between immunity and stem cells in health and disease. Cell 2018;175:908–920.

26. Woolf E, Xiao C, Fainaru O, Lotem J, Rosen D, Negreanu V, Bernstein Y, Goldenberg D, Brenner O, Berke G, Levanon D, Groner Y. Runx3 and Runx1 are required for CD8 T cell development during thymopoiesis. Proc Natl Acad Sci U S A 2003;100:7731–7736.

27. Milner JJ, Toma C, Yu B, Zhang K, Omilusik K, Phan AT, Wang D, Getzler AJ, Nguyen T, Crotty S, Wang W, Pipkin ME, Goldrath AW. Runx3 programs CD8(+) T cell residency in non-lymphoid tissues and tumours. Nature 2017;552:253–257.

28. Osaki LH, Bockerstett KA, Wong CF, Ford EL, Madison BB, DiPaolo RJ, Mills JC. Interferon-gamma directly induces gastric epithelial cell death and is required for progression to metaplasia. J Pathol 2019; 247:513–523.

29. Vecchi M, Nuciforo P, Romagnoli S, Confalonieri S, Pellegrini C, Serio G, Quarto M, Capra M, Roviaro GC, Contessini Avesani E, Corsi C, Coggi G, Di Fiore PP, Bosari S. Gene expression analysis of early and advanced gastric cancers. Oncogene 2007; 26:4284–4294.

30. Goldenring JR, Nam KT, Mills JC. The origin of pre-neoplastic metaplasia in the stomach: chief cells emerge from the Mist. Exp Cell Res 2011; 317:2759–2764.

31. Craig SW, Powell LD. Regulation of actin polymerization by villin, a 95,000 Dalton cytoskeletal component of intestinal brush borders. Cell 1980;22:739–746.

32. Matsuo J, Douchi D, Myint K, Mon NN, Yamamura A, Kohu K, Heng DL, Chen S, Mawan NA, Nuttonmanit N, Li Y, Srivastava S, Ho SWT, Lee NYS, Lee HK, Adachi M, Tamura A, Chen J, Yang H, Teh M, So JB, Yong WP, Tan P, Yeoh KG, Chuang LSH, Tsukita S, Ito Y. Iqgap3-Ras axis drives stem cell proliferation in the stomach corpus during homoeostasis and repair. Gut 2021; 70:1833–1846.

33. Sato T, Ishikawa S, Asano J, Yamamoto H, Fujii M, Sato T, Yamamoto K, Kitagaki K, Akashi T, Okamoto R, Ohteki T. Regulated IFN signalling preserves the stemness of intestinal stem cells by restricting differentiation into secretory-cell lineages. Nat Cell Biol 2020; 22:919–926.

34. Ryl T, Kuchen EE, Bell E, Shao C, Florez AF, Monke G, Gogolin S, Friedrich M, Lamprecht F, Westermann F, Hofer T. Cell-cycle position of single MYC-driven cancer cells dictates their susceptibility to a chemotherapeutic drug. Cell Syst 2017;5:237–250 e8.

35. Pardee AB. A restriction point for control of normal animal cell proliferation. Proc Natl Acad Sci U S A 1974; 71:1286–1290.

36. Love NK, Keshavan N, Lewis R, Harris WA, Agathocleous M. A nutrient-sensitive restriction point is active during retinal progenitor cell differentiation. Development 2014;141:697–706.

37. Lee JW, Kim DM, Jang JW, Park TG, Song SH, Lee YS, Chi XZ, Park IY, Hyun JW, Ito Y, Bae SC. RUNX3 regulates cell cycle-dependent chromatin dynamics by functioning as a pioneer factor of the restriction-point. Nat Commun 2019;10:1897.

38. Chi XZ, Lee JW, Lee YS, Park IY, Ito Y, Bae SC. Runx3 plays a critical role in restriction-point and defense against cellular transformation. Oncogene 2017; 36:6884–6894.

39. Bae SC, Kolinjivadi AM, Ito Y. Functional relationship between p53 and RUNX proteins. J Mol Cell Biol 2019; 11:224–230.

40. Lee JW, Park TG, Bae SC. Involvement of RUNX and BRD family members in restriction point. Mol Cells 2019; 42:836–839.

41. Martinsson HS, Starborg M, Erlandsson F, Zetterberg A. Single cell analysis of G1 check points-the relationship between the restriction point and phosphorylation of pRb. Exp Cell Res 2005;305:383–391.

42. Karam SM, Leblond CP. Dynamics of epithelial cells in the corpus of the mouse stomach. I. Identification of proliferative cell types and pinpointing of the stem cell. Anat Rec 1993;236:259–279.

43. Stoeber K, Tlsty TD, Happerfield L, Thomas GA, Romanov S, Bobrow L, Williams ED, Williams GH. DNA replication licensing and human cell proliferation. J Cell Sci 2001;114:2027–2041.

44. Carroll TD, Newton IP, Chen Y, Blow JJ, Nathke I. Lgr5(+) intestinal stem cells reside in an unlicensed G1 phase. J Cell Biol 2018;217:1667–1685.

45. Willet SG, Lewis MA, Miao ZF, Liu D, Radyk MD, Cunningham RL, Burclaff J, Sibbel G, Lo HG, Blanc V, Davidson NO, Wang ZN, Mills JC. Regenerative proliferation of differentiated cells by mTORC1-dependent paligenosis. EMBO J 2018;37:e98311.

46. Miao ZF, Sun JX, Adkins-Threats M, Pang MJ, Zhao JH, Wang X, Tang KW, Wang ZN, Mills JC. DDIT4 licenses only healthy cells to proliferate during injury-induced metaplasia. Gastroenterology 2021;160:260–271 e10.

47. Ito K. RUNX3 in oncogenic and anti-oncogenic signaling in gastrointestinal cancers. J Cell Biochem 2011; 112:1243–1249.

48. Kitajima Y, Ohtaka K, Mitsuno M, Tanaka M, Sato S, Nakafusa Y, Miyazaki K. Helicobacter pylori infection is an independent risk factor for Runx3 methylation in gastric cancer. Oncol Rep 2008;19:197–202.

49. Liu Z, Xu X, Chen L, Li W, Sun Y, Zeng J, Yu H, Chen C, Jia J. Helicobacter pylori CagA inhibits the expression of Runx3 via Src/MEK/ERK and p38 MAPK pathways in gastric epithelial cell. J Cell Biochem 2012;113:1080–1086.

50. Fernandez-Alonso R, Davidson L, Hukelmann J, Zengerle M, Prescott AR, Lamond A, Ciulli A, Sapkota GP, Findlay GM. Brd4-Brd2 isoform switching coordinates pluripotent exit and Smad2-dependent lineage specification. EMBO Rep 2017;18:1108–1122.

51. Caputo VS, Trasanidis N, Xiao X, Robinson ME, Katsarou A, Ponnusamy K, Prinjha RK, Smithers N, Chaidos A, Auner HW, Karadimitris A. Brd2/4 and Myc regulate alternative cell lineage programmes during early osteoclast differentiation in vitro. iScience 2021;24:101989.

52. Sigal M, Rothenberg ME, Logan CY, Lee JY, Honaker RW, Cooper RL, Passarelli B, Camorlinga M, Bouley DM, Alvarez G, Nusse R, Torres J, Amieva MR. Helicobacter pylori activates and expands Lgr5(+) stem cells through direct colonization of the gastric glands. Gastroenterology 2015;148:1392–1404 e21.

53. Matsuo J, Kimura S, Yamamura A, Koh CP, Hossain MZ, Heng DL, Kohu K, Voon DC, Hiai H, Unno M, So JB, Zhu F, Srivastava S, Teh M, Yeoh KG, Osato M, Ito Y. Identification of stem cells in the epithelium of the stomach corpus and antrum of mice. Gastroenterology 2017;152:218–231 e14.

54. Seo W, Taniuchi I. The roles of RUNX family proteins in development of immune cells. Mol Cells 2020;43:107–113.

55. Yagi T, Tokunaga T, Furuta Y, Nada S, Yoshida M, Tsukada T, Saga Y, Takeda N, Ikawa Y, Aizawa S. A novel ES cell line, TT2, with high germline-differentiating potency. Anal Biochem 1993;214:70–76.

56. Lakso M, Pichel JG, Gorman JR, Sauer B, Okamoto Y, Lee E, Alt FW, Westphal H. Efficient in vivo manipulation of mouse genomic sequences at the zygote stage. Proc Natl Acad Sci U S A 1996;93:5860–5865.

57. Dobin A, Davis CA, Schlesinger F, Drenkow J, Zaleski C, Jha S, Batut P, Chaisson M, Gingeras TR. STAR: ultrafast universal RNA-seq aligner. Bioinformatics 2013;29:15–21.

58. Liao Y, Smyth GK, Shi W. The Subread aligner: fast, accurate and scalable read mapping by seed-and-vote. Nucleic Acids Res 2013;41:e108.

59. Robinson MD, McCarthy DJ, Smyth GK. edgeR: a Bioconductor package for differential expression analysis of digital gene expression data. Bioinformatics 2010; 26:139–140.

60. Chua SW, Vijayakumar P, Nissom PM, Yam CY, Wong VV, Yang H. A novel normalization method for effective removal of systematic variation in microarray data. Nucleic Acids Res 2006;34:e38.

Correspondence
Address correspondence to: Yoshiaki Ito, MD, PhD, or Linda Shyue Huey Chuang, PhD, Cancer Science Institute of Singapore, National University of Singapore, 14 Medical Drive #12-01, Singapore 117599. e-mail: csicshl@nus.edu.sg; csiitoy@nus.edu.sg; fax: (65) 6873-96-64.